Coastal Engineering 107 (2016) 84–101

Contents lists available at ScienceDirect

Coastal Engineering

journal homepage: www.elsevier.com/locate/coastaleng

# A temporal waterline approach to mapping intertidal areas using X-band marine radar

Paul S. Bell [a,*], Cai O. Bird [b], Andrew J. Plater [b]

[a] National Oceanography Centre, Liverpool, United Kingdom
[b] University of Liverpool, School of Environmental Science, United Kingdom

ARTICLE INFO

*Article history:*
Received 5 March 2015
Received in revised form 19 June 2015
Accepted 7 September 2015
Available online xxxx

*Keywords:*
Remote sensing
Marine radar
Waterline
Intertidal mapping
Coastal monitoring

ABSTRACT

Mapping the morphology of intertidal areas is a logistically challenging, time consuming and expensive task due to their large expanse and difficulties associated with access. A technique is presented here that uses standard marine navigational radar operating at X-band frequency. The method uses a series of time-exposure radar images over the course of a two-week tidal cycle to identify the elevation of the wetting and drying transitions at each pixel in the radar images, thereby building up a morphological map of the target intertidal area. This "Temporal Waterline" method is applied to a dataset acquired from Hilbre Island at the mouth of the Dee Estuary, UK, spanning March 2006 to January 2007. The radar gathered data with a radial range of 4 km and the resulting elevation maps describe the intertidal regions of that area. The results are compared with airborne LiDAR data surveyed over the same area and within the radar survey time period. The residual differences show good agreement across large areas of beach and sandbanks, with concentrations of poor estimations around points that are shadowed from the radar or likely to suffer from pooling water. This paper presents the theoretical framework of the method and demonstrates its stability and accuracy. The Temporal Waterline radar method is aimed at providing a useful tool for the monitoring and operational management of coastlines.



## 1. Introduction

### 1.1. The importance of mapping intertidal morphology

Coastal, shallow water environments are important to commercial activities as they are often the site of ports, harbours and recreational areas which represent high value assets in the provision of various ecosystem services and are the foundation of many local and national economies. These shallow water systems are also incredibly dynamic and their morphology is known to change significantly during high energy storm events, and more gradually during average conditions. The nature, extent and timescales of such changes at a variety of intertidal areas around the world have been well documented (Fisher and Stauble, 1977; Fitzgerald et al., 1994; Morton et al., 1995; Nicholls and Marston, 1939; Sexton and Moslow, 1981; Stone et al., 1996). Changes in morphology can compromise navigation channels and inlets in a variety of ways (FitzGerald et al., 2000) and can have significant financial consequences; the United States spends more than $100 million annually on Federal channel maintenance, dredging between 50 and 100 million $m^3$ of sand (Rosati and Kraus, 2000).

At a regional level, strategic ports located in morphologically dynamic areas such as river deltas can experience significant navigation channel disruption due to sedimentation. An example of this is Port Harcourt located in the Bonny River estuary which empties into the Niger Delta region, Nigeria. This Port is a crucial gateway to the oil-producing region, and the complicated system of sandbars and shoals combined with dynamic bank and shoreline erosion present navigational risks to shipping operating in the vicinity of the port. Often the series of exposed jetties in the Bonny River estuary are isolated as the shoreline is eroded (Diop et al., 2014). This area is too large and exposed to monitor manually with ease and therefore a method of remotely monitoring the health and morphology of the coastline in dynamic areas such as this could be highly effective. Another example of a vulnerable area is the mouth of the Amazon River, where sandbanks are known to encroach upon the critical navigation channels. Sand bank migration rates of up to 250 m/year have been observed here (Fernandes et al., 2007), causing significant disruption to the operation of the ports.

At a more focussed, local scale the Port of Liverpool in the UK removed an average of 1.86 million tonnes of dredged sediment annually between 2005 and 2009. This material was extracted from the navigation channel and berthing zones, areas which are known to be significantly influenced by migrating sedimentary bed features (Bailey, 2009). Migration of allochthonous sediment into estuaries is a prevalent problem in port management, specifically in estuaries where ports are

* Corresponding author at: National Oceanography Centre, Joseph Proudman Building, 6 Brownlow Street, Liverpool, L3 5DA.
*E-mail address:* psb@noc.ac.uk (P.S. Bell).

http://dx.doi.org/10.1016/j.coastaleng.2015.09.009

present. The changing sediment budget combined with climate change-induced rising sea level and changing bathymetry could result in the "squeezing out" of valuable intertidal habitats that lie between hard sea defences and the shoreline (De Vriend et al., 2011). Experiments have been conducted involving the disposal of dredged material at eroding beach sites in order to supply sediment replacement (van der Wal et al., 2011). Schemes such as this, along with planned and ongoing large-scale sand-scaping/sand engine operations in the UK and Holland (Stive et al., 2013), also see Zandmotor (http://www.dezandmotor.nl/en-GB/), which seek to change the shape of a coastline in order to increase the socio-economic potential of the area, would benefit greatly from a cost-effective method of long-term intertidal monitoring. In addition, significant cost savings and improvements in the efficiency of dredging operations and coastal defence construction may be made through wide area intertidal surveillance and prediction of large-scale sediment migration. This paper describes and presents a novel technique for mapping the changes in intertidal coastal morphology across varying timescales using standard marine radar operating at X-band, providing much needed situational awareness in intertidal areas and utilising existing port infrastructure, whilst keeping operational costs to a minimum.

### 1.2. Current methods of surveying intertidal areas

The task of surveying intertidal areas has traditionally been performed using well established survey methods. When the water level is sufficiently high, shallow draught vessels fitted with echosounders may be used, and when the water level is low enough to expose the area, survey lines may be walked by a surveyor equipped with a high accuracy GPS system or driven via a GPS equipped all-terrain vehicle. The use of vessel-based multibeam echo sounder surveys is constrained by expense and inefficiency of operation over large areas and the limited swath width in shallow waters (Gao, 2009). Airborne LiDAR (Light detection and ranging, Lyzenga (1985)) is a non-imaging technique using laser pulses to detect the range to the ground at low water or the water surface in wet areas. More advanced versions can distinguish the signals from the water surface and the secondary reflection from the sea bed providing water clarity is sufficiently good. In recent years, airborne LiDAR has become the tool of choice for surveying large intertidal areas and multiple surveys flown over the same area can be used to accurately monitor changes in bathymetry (Guenther et al., 2000). Although these techniques have improved significantly in accuracy and applicability over recent decades, they remain expensive, relatively time consuming and rarely run over the same area on a routine basis. Consequently, data recorded in dynamic areas quickly becomes obsolete until the next survey. When used in this manner these methods provide only snapshots of episodic morphological change over relatively long timescales. In order to complement these accurate and focused surveys, a method that provides constant, long-term monitoring over a wide area of the coast would provide unprecedented insight into the episodic, seasonal and interannual variability of intertidal areas.

An effective and long-established method of monitoring shoreline position and nearshore beach processes is to use video camera analysis of the nearshore and swash zones (Aarninkhof et al., 2003, 2005; Holland et al., 1997; Holman and Stanley, 2007; Holman et al., 1993; Plant and Holman, 1997; Santiago et al., 2013; Sobral et al., 2013). Video monitoring has been used successfully to monitor stretches of intertidal beach at a number of sites around the world, such as during a large European research project CoastView (Davidson et al., 2007) and improvements continue to be made, including automated methods that are capable of updating bathymetric maps on a daily basis (Uunk et al., 2010). The use of thermal infrared cameras allows such methods to be performed using data collected both during the day and at night to derive intertidal DEM (Digital Elevation Models) (Gaudin et al., 2009). Video cameras mounted on towers along a shoreline have also been used successfully in combination with in situ sensors to measure morphological change and sediment transport (Austin and Masselink, 2006) and these passive optical sensors have been proven to be accurate and effective in their deployment.

### 1.3. Depth mapping with marine X-band radar

Marine radar generally operates well in low visibility, has excellent temporal and spatial coverage and is able to provide similar data to that of a camera at slightly lower resolution but to a significantly greater range and regardless of light conditions (Dankert and Horstmann, 2007). X-band radar has become an integral part of the nearshore remote sensing infrastructure in recent years (Holman and Haller, 2013). Operationally, it has been used extensively to determine 2-D wave spectra in offshore areas for both commercial and scientific applications for many years now (Nieto Borge and Guedes Soares, 2000; Reichert et al., 1999), for the most part using techniques based on those developed by Young et al. (1985). The visibility of ocean waves on the radar imagery and the ability to record sequences of these images of the waves allow their wavelength and period to be determined. If currents are neglected, various techniques can be used to fit the water depth that best explains the observed wave behaviour (Bell, 1999, 2008; Bell et al., 2006; Flampouris et al., 2009; Hessner et al., 1999).

If the data are from areas where currents cannot be neglected, it becomes necessary to find the best fit to the location of the wave dispersion surface in the full 3D wavenumber-frequency domain in terms of the water depth and the two components of the current vector. Again, there are various approaches to both determining (and sometimes filtering) the frequency wavenumber spectrum and also a number of approaches in finding the best fit of the current vector and depth to the observed wavenumber spectrum (Hessner and Bell, 2009; Hessner et al., 2014; Nieto Borge et al., 2004, 2008; Senet et al., 2008; Serafino et al., 2010). Such techniques have been used successfully to map currents at tidal energy test sites in Scotland UK (Bell et al., 2012; McCann and Bell, 2014). Recently, the additional complication of correcting for vessel movement has started to be addressed in order to allow bathymetry mapping using radar data from a moving vessel, and water depth maps down to a water depth of approximately 50 m have been shown to be possible (Bell and Osler, 2011).

The overriding stipulation for these wave inversion techniques is that clear wave fields must be visible to the radar in order for the analysis to work accurately. Such techniques also inherently involve the analysis of data windows of several hundred metres square in order to allow the determination of the wave properties required to reliably determine both water depth and currents. Thus a degree of spatial averaging is involved that makes that approach less useful for the mapping of often high spatially variable intertidal areas.

The Temporal Waterline method detailed in the following sections is not as reliant on the presence of coherent wave patterns on the radar data and operates at a pixel level rather than involving spatial averaging. The combination of the products of water line and wave inversion methodologies is planned for future work.

### 1.4. The Temporal Waterline method

The method presented in this paper builds upon known principles, an early version of which was described by Admiral Sir R.H. Bacon who commanded the UK Dover Patrol from 1915–1917. During this time he correctly theorised that aerial photographs taken at regular timed intervals over a shoreline could be used in conjunction with known tidal levels measured from a submarine to create a series of contour lines that described elevations above Chart Datum, and thus describe the beach profile (Bacon, 1932). This knowledge was critical in the planning of amphibious landings and military operations in the nearshore area. This underlying principle has been applied to a variety of remote sensing methods, such as Synthetic Aperture Radar (SAR) by Koopmans and Wang (1994) who picked out the waterlines of the

intertidal areas of the Wadden Sea and assigned those contours to water elevations based on a tidal model. Mason et al. (1995) carried out a similar exercise with SAR images of the extensive intertidal regions of the Morecambe Bay area of the UK. An iterative process was later used between the tidal model and updating bathymetry to arrive at more precise tidal elevations for the detected waterlines (Annan, 2001).

The waterline approach to intertidal mapping has also been applied to marine radar data. Takewaka (2005) showed that beach elevations could be determined by associating the strong radar echo due to waves breaking on the shoreline with the tidal elevation recorded nearby. Beach slopes were also calculated from a number of records separated in time. However, the analysis used by Takewaka sometimes required manual intervention to correct the waterline estimate and hence was inappropriate for automated application to large datasets and long time-series.

Repeated analysis of the same area over varying timescales allows the measurement and quantification of sediment transport (Mason and Garg, 2001; Mason et al., 1999; Ryu et al., 2008). The source of images is commonly SAR from either satellite or survey aircraft, because the active sensing ability of SAR allows penetration of cloud cover and the gathering of images during poor weather, a quality shared by X-band radar. It is also possible to use traditional optical satellite images to detect waterlines (Ryu et al., 2002), the availability of which can be intermittent, thus reducing the temporal resolution of the method and leading to increased interpolation errors in the final map. Recently this method has been used to map large areas of the coast of China with mean vertical errors in the measurements between 29 and 42 cm (Liu et al., 2013). The technique was also applied using SAR images to map the change in topography on tidal flats along the Wadden Sea German coast between 1996 and 1999. The elevation values in this region were compared to those gathered by survey vessel, the mean error was 20 cm in 1996 and 21 cm in 1999 (Heygster et al., 2010).

The X-band radar waterline method described here differs from those already discussed by moving the waterline detection from the spatial domain of identifying the discrete waterline in individual images, to the temporal domain where the transitions between wet and dry are associated with the best match between pixel intensity records and the tidal signal which would cause that wetting/drying pattern over a given time period (Bell, 2014). This takes advantage of the excellent temporal update rates possible with ground-based remote sensing but could equally be applied to a range of remote sensing data types, given a sufficient number of images. More importantly, it circumvents the need for the waterlines in individual images to be clear and unambiguous — which is often not the case. Most published methods contain extensive details of error correction methods to deal with discontinuities in contour lines in individual images or handle ambiguous water lines. With the temporal approach these are unnecessary, and thus the method is easily automated and inherently more robust.

## 2. Methodology

### 2.1. Experiment description

Radar image data were collected using a Kelvin Hughes 9.4 GHz horizontally polarised X-band marine radar mounted on a 15 m mast (Fig. 1), itself approximately 15 m above chart datum, at Hilbre Island, northwest UK at the mouth of the River Dee (Fig. 2). This site offers good visibility of the estuary and the north western beach of the Wirral peninsula. The Dee estuary is a funnel-shaped, macrotidal estuary on the border between North Wales and England with a maximum spring tidal range of more than 10 m. The site features particularly interesting geomorphology, with a progressively accreting saltmarsh to the south-east, migrating tidal channels within the central sandbanks and shifting intertidal bed features along the beach. The waves within Liverpool Bay and the mouth of the Dee estuary are locally generated and fetch limited within the eastern Irish Sea such that significant wave height ($H_s$) is less than 5.5 m, the peak wave period ($T_p$) is less than 12 s, and the mean period less than 8 s (Wolf et al., 2011). The main channel of the River Dee splits into two deep channels around 12 km downstream from a canalised section leading to the City of Chester, the Hilbre channel to the east and the Welsh channel to the west, which feed into the Eastern Irish Sea (Moore et al., 2009).

**Fig. 1.** A photo of the radar tower looking north on Hilbre Island.

### 2.2. Radar data collection and pre-processing

Hilbre Island, where the radar was located, is cut off from the mainland for the upper half of every tidal cycle and has no grid-connected electricity supply. In order to provide power to the ranger station on the island, a 2 kW wind turbine and off-grid battery storage system with diesel generator back-up was installed by Wirral Borough Council, which provided power most of the time. The remote nature of the site made maintenance and monitoring of both the power systems and the radar system a challenge and numerous gaps exist in the dataset as a result. Despite these challenges, several years of radar data were collected before a number of factors made the data collection impractical to continue.

The radar data used in the present work were gathered over 10 months from March 2006 to January 2007. Further archives of radar data up to 2009 exist and will form the basis of future work investigating episodic, seasonal and interannual changes within the estuary. The 2.4 m radar antenna was mounted approximately 30 m above chart datum and set to short pulse (~60 ns pulse length) in order to cover a 4 km range radius. The data were then sampled at 40 MHz with a radial resolution of 3.75 m using an OceanWaves GmbH Wamos system linked to the internet via a long range wi-fi link to the mainland. The antenna rotated at 25 rpm yielding an image every 2.4 s. The raw data were then interpolated from polar coordinates onto a Cartesian grid to enable georeferencing and proper visualisation of the results. This process includes the removal of small variations in antenna rotation rate that

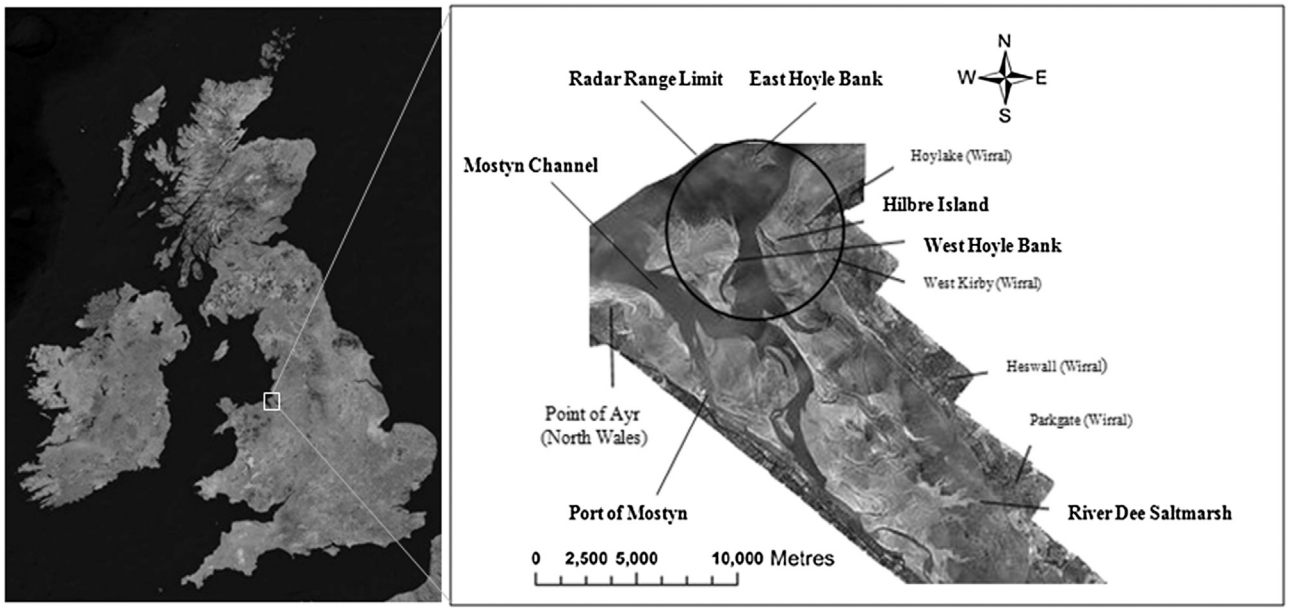


**Fig. 2.** Study area showing key points in the Dee Estuary with radar location and range.

would otherwise cause an azimuthal error of several degrees in the location of nominally static targets if a uniform antenna rotation rate was assumed.

Strictly speaking, the polar to Cartesian conversion should also account for the slant range associated with the elevation of the radar antenna above ground level — a simple calculation using Pythagoras' theorem. However, as the ground level is the unknown quantity in this analysis, one can either assume an approximate elevation that accounts for the majority of the slant range error or include no correction. The option of no correction was chosen in this case as an antenna elevation of approximately 25–30 m coupled with a Cartesian pixel size of 5 m means that the slant range error only becomes greater than the pixel size for points within approximately 100 m of the radar in a region where data is being recorded to a range of almost 4 km.

If precision over the nearest 100 m was of principle concern, the simplest method would be to perform the waterline method with no slant range correction, and once the elevation of each pixel had been identified, apply a correction to the radial range of each pixel based on the slant range appropriate to that elevation and range. A detailed correction for this effect was considered an unnecessary over-complication in the present work considering the likely marginal gains in positional accuracy. It may however be implemented as a refinement in future work if necessary.

Images produced from radar data show not only detected hard targets such as ships and land, but also many reflections from the sea surface. This is known generally as “sea clutter” and is a product of Bragg scattering from centimetre-scale capillary waves on the sea surface interacting with the projected electromagnetic energy (Valenzuela, 1978) and sea spikes, a scattering phenomenon occurring when radar waves interact with steep or breaking waves at low grazing angles (Coakley et al., 2001; Fuchs et al., 1999; Ja et al., 2001; Trizna et al., 1991). This sea clutter is inconsequential for the most part if wind speed is low (<3 m/s). As the sea surface is not roughened sufficiently, significant wave heights less than 1 m are also difficult to detect with radar. This radar frequency is also used by weather radars and thus rainfall is also visible on marine X-band radar and can potentially obscure the sea clutter (Bell et al., 2012). Fig. 3 shows a snapshot of radar image data collected from Hilbre Island. The hard coast of the Wirral mainland is clearly defined to the east and sea clutter is also detected, particularly along the shoreline to the northeast where breaking waves give higher radar returns.

The intensity of a pixel in a radar image is dependent on the strength of the radar returns from that location (Richards, 2005) and in marine radars is uncalibrated and usually logarithmically amplified. The raw value of the returned signal is stored as an unsigned 12-bit integer by the particular digitisation system used here.

Sequential radar images recorded once per antenna rotation provide movies of waves (when visible) propagating up to the shore, and the interface between wet areas and dry areas varies from wave to wave. In order to stabilise this fluctuating signal and define a “waterline” representative enough for this analysis, the radar images from each 10 min burst (of 256 images) are temporally averaged, smoothing the wave signatures and yielding an image that is analogous to a time-exposure in photography, in which the limit of the interface between land and ocean is more easily distinguished (Fig. 4). The time exposure radar

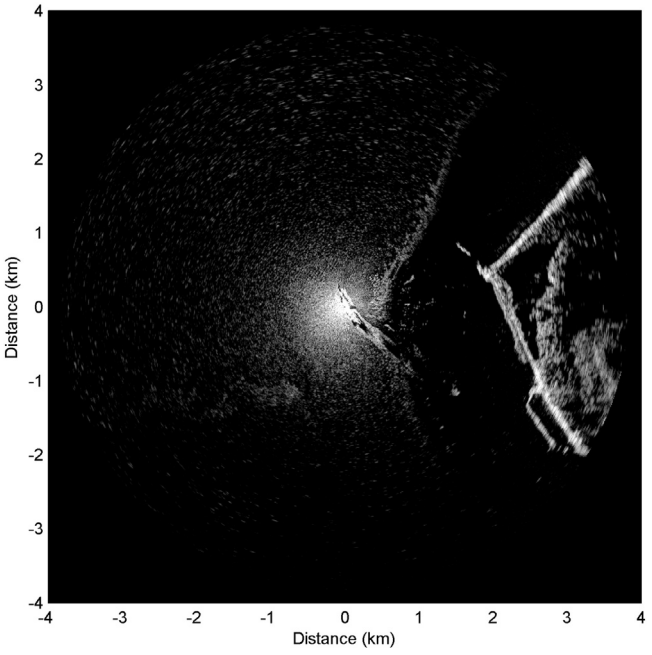


**Fig. 3.** Snapshot radar image from Hilbre Island showing high returns from the coastline and breaking waves along the waterline.

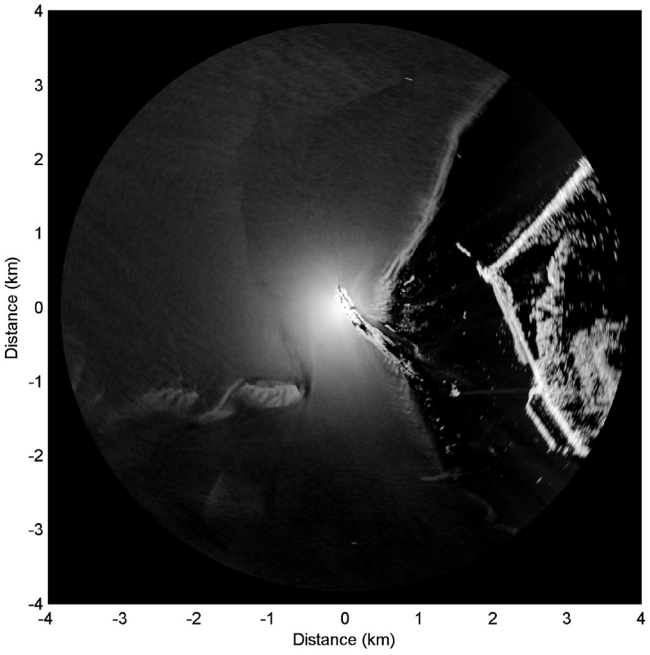


**Fig. 4.** Time exposure radar image representing ten minutes of data showing general patterns of wave breaking and sea clutter.

images used in this work represent just over 10 min of data that were gathered either every hour or every 30 min, depending on the operating regime. Fig. 4 shows a sample time exposure image used in this method. This image represents a period at low tide and so a great deal of beach is exposed between the shoreline and the seawalls and dunes along the peninsula to the east of Hilbre Island. The tidal sandbanks to the west are also exposed at low tide and the repeated wave breaking along the margins of the Hilbre channel picks out the general shape of the sandbank margins.

### 2.3. Tidal elevation data

The aim of the presented method is to map the intertidal area, which follows a cycle of wetting and drying governed primarily by the tides and varied local beach morphology. A partial record of tidal elevation was available from an old tide gauge located on the northernmost tip of Hilbre Island close to where the radar was located. This tide gauge, which has existed in various forms for up to 130 years, was refurbished in its present form by the Mersey Docks and Harbour Corporation (now Peel Ports) during the 1970s. It consisted of an obsolete float gauge with chart plotter. The stilling well for the float was cut into the sandstone bedrock of the island and connected to a subtidal location off the northern end of the island via a lead pipe. A pressure sensor was also located in the stilling well coupled to a VHF transmitter from which data were automatically relayed to both the Mersey Docks and Harbour Corporation and to the Proudman Oceanographic Laboratory (now the National Oceanography Centre). When the Proudman Oceanographic Laboratory moved from its original site at Bidston Observatory to Liverpool in 2004, the range became too great for line of sight reception of the VHF signal, so a VHF receiver was connected directly to the radar digitiser PC on Hilbre Island to pick up the tide gauge data from then on whenever the radar was operating. Unfortunately the inlet pipe had degraded and became increasingly prone to blockages and siltation in recent years, compromising data quality. It was finally discontinued by Peel Ports in favour of an offshore radar level gauge in 2010.

The available Hilbre Island tide gauge data is shown in Fig. 5a with the period that overlaps with the study period of the present work shown in blue. Fig. 5b shows the residual when the tidal prediction for Hilbre Island is removed from the tide gauge record. There are clear anomalies in various parts of the record that become obvious in the residuals, notably in spring 2007, towards the end of 2007, and finally showing almost complete blockage of the system in mid-2008.

The incomplete and at times unreliable nature of the tidal record made it unsuitable for use in this application where a robust and continuous time series of water levels was required. An alternative approach was therefore adopted taking advantage of the nearest UK National Tide Gauge Network class 'A' tide gauge outside Gladstone Dock, Liverpool. The residual meteorological contribution to the tide at Liverpool was determined by subtracting the predicted tide from the measured tide. This is shown in Fig. 5c with the period corresponding to the present study highlighted in blue. The assumption was made that this meteorological component of the water level was a geographically wide area effect that could also be used as an approximation for the meteorological component of the water level at Hilbre Island, 15 km to the west. This was then added to the predicted tide for Hilbre Island to provide the required water level for the radar waterline analysis, shown in Fig. 5d with the study period again highlighted in blue. In order to verify that this "synthetic tide" was a better representation of the water elevation than tide predictions alone, tidal records from mid-September 2006 to mid-February 2007 were subjectively selected as a period when the Hilbre Island tide gauge was not suffering from significant issues with pipe blockages — i.e. when obvious anomalies in the tide gauge data and residuals were not evident. It should be noted that the authors cannot be certain that even this section of the data was not contaminated by pipe blockages, only that any such effects were small.

The tidal residuals for both Liverpool Gladstone Dock and Hilbre Island were calculated by subtracting the tidal predictions from the measured water levels. As expected, a scatter plot of the residuals from one gauge compared with the other in Fig. 6 shows a strong linear relationship between the residuals from the two tide gauges, with an $R^2$ correlation of 0.9, a standard deviation of less than 0.10 m and a Root Mean Square (RMS) difference of 0.10 m.

Over the same period, the RMS tidal residual of the Gladstone Dock data was 0.37 m, suggesting that if a similar residual was present on the Hilbre water levels then addition of the tidal residual from Gladstone Dock to the tidal prediction for Hilbre Island should provide a significantly more accurate water level than using predictions alone. The residuals from the Hilbre tide gauge data with respect to the tidal predictions alone were compared with the remaining signal when the synthetic tide (comprising the Hilbre tidal prediction plus the Gladstone Dock residual) were subtracted, shown in Fig. 5e. With predictions alone, the Hilbre Island RMS residual for the test period of September 2006–February 2007 was found to be 0.38 m, whilst the use of the synthetic tide was found to reduce this to 0.1 m. This represents a reduction in the difference of almost a factor of 4, confirming that this approach of adding the residual from the Liverpool tide gauge to that of the Hilbre Island tidal predictions yields a significantly more accurate representation of the water levels at that site than predictions alone. A subsection of the tidal data are shown in Fig. 7, with the tide prediction marked as the red dotted line, the Hilbre tide gauge data, which was considered valid during that period, marked in blue, and the synthetic tide marked as the black dots. The points marking the synthetic tide can be seen to overlay the tide gauge data (cyan line) almost perfectly.

### 2.4. LiDAR ground truth survey

An aerial LiDAR survey of the majority of the Dee Estuary was conducted by the UK Environment Agency on the 8th of October 2006, shortly after a significant wave event. The survey was conducted using an Optech ALTM 3100 LiDAR system flown by a dedicated survey aircraft at an altitude of approximately 900 m. A total of 20 flight lines were flown to cover the estuary between 04:25 and 07:26 GMT during which the tidal elevations ranged from 0.72 m to 2.47 m, shown as the region shaded in grey on Fig. 7. Calibration flights were carried out at

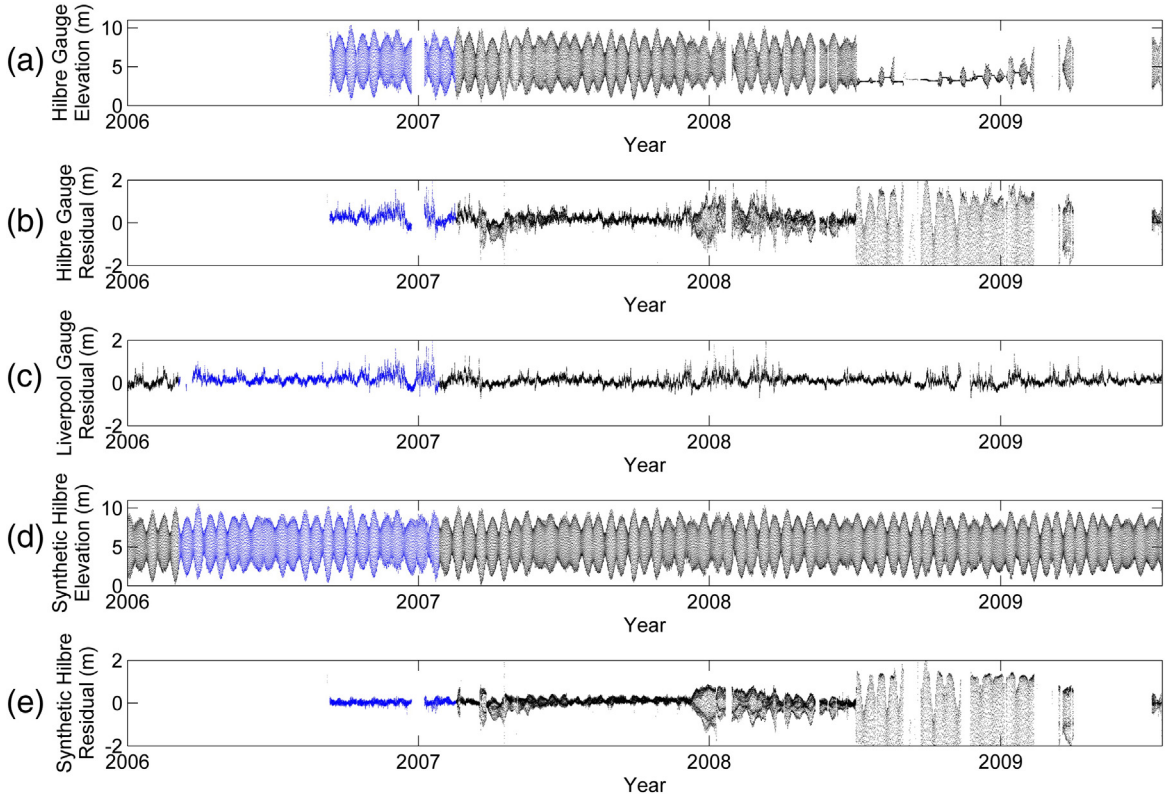


**Fig. 5.** (a) The Hilbre Island tide gauge data from September 2006 to summer 2009. The region plotted in blue relates to the present study period; (b) the Hilbre Island tidal residual calculated with respect to a tidal prediction; (c) the class 'A' Liverpool Gladstone Dock tide gauge residual; (d) the Hilbre Island synthetic tide constructed from the tidal prediction + the Gladstone Dock residual. The region plotted in blue represents the period spanning the present study; (e) the Hilbre Island residual with respect to the Hilbre Island synthetic tide. (For interpretation of the references to colour in this figure legend, the reader is referred to the web version of this article.)

regular intervals by the system operators and the last calibration flight prior to this survey was reported to be in June 2006. The accuracy of this instrument at altitudes of up to 1200 m is quoted by the manufacturer as 0.15 m or better (1 × standard deviation) with a range resolution of 0.01 m. A ground truth survey conducted by the Environment Agency as part of this survey showed a root mean square error of 0.071 m between the LiDAR survey and a GPS ground survey, comprising a systematic error (bias) by the LiDAR data of −0.052 m and a random error of 0.097 m. These comparisons were within acceptable tolerance for that instrument.

The LiDAR elevation data were supplied as a gridded dataset with a 1 m horizontal pixel size. Reflectivity data were also supplied in a similar format. In order to more closely match the resolution of the radar data, the 1 m gridded elevation data from the LiDAR were mean gridded on a

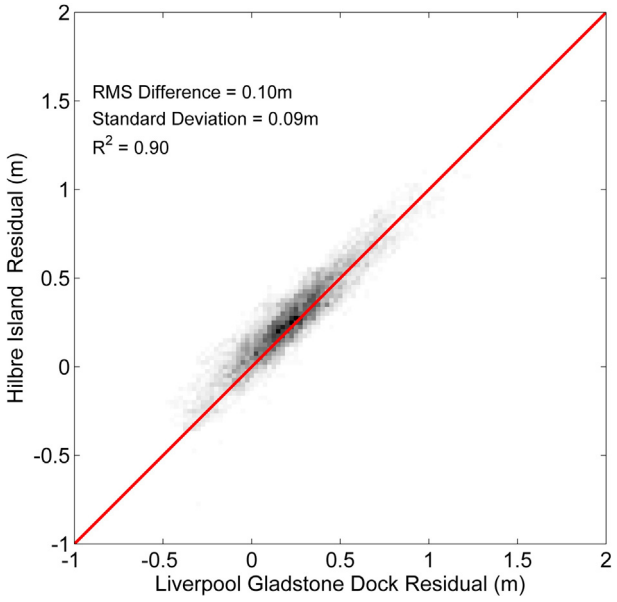


**Fig. 6.** The tidal residuals (measured minus predicted) for Hilbre Island compared with Liverpool Gladstone Dock showing a strong $R^2$ of 0.9.

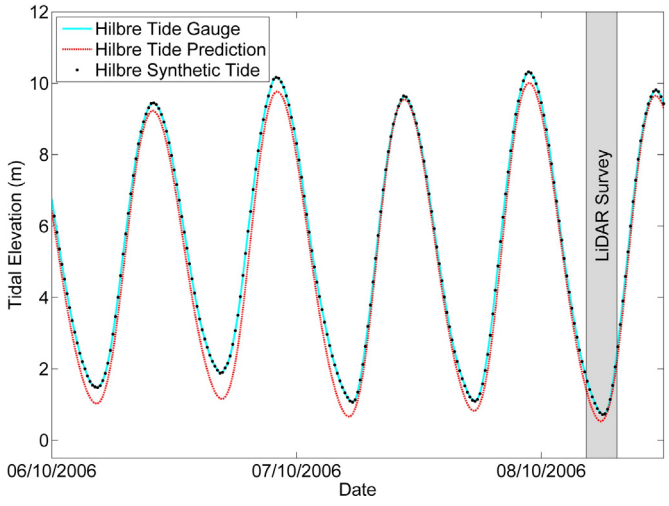


**Fig. 7.** A subsection of the tidal data for Hilbre Island, with the tide prediction marked as the red dotted line, the Hilbre tide gauge data which was considered valid during that period, marked in cyan, and the synthetic tide marked as the black dots. The highlighted grey area corresponds to the period during which the LiDAR survey was flown. (For interpretation of the references to colour in this figure legend, the reader is referred to the web version of this article.)

5 m grid and elevations were adjusted from Ordinance Datum Newlyn (ODN) to Admiralty Chart Datum (ACD) corresponding approximately to Lowest Astronomical Tide by adding 4.93 m to the ODN values for the comparisons presented here.

Examination of the original 1 m gridded data showed clear evidence of elevations related to the water surface in wet areas, thus elevation values below 2.5 m relative to chart datum were eliminated from the comparison as potentially contaminated data points. Examination of the reflectivity values in these wet areas showed high reflectivity when the laser beam was pointing near vertical, and very low reflectivity data at lower grazing angles. Features with similar reflectivity signatures could be identified by eye in the bottom of channels in the sand flats and sand banks, indicating a strong likelihood that such areas contained pooling water, even near low tide when the survey was conducted. Filtering out such areas from the LiDAR survey was not attempted as no unique criteria could be determined for that purpose.

## 3. The temporal waterline method

The initial step in this method is to gather time series of individual radar pixel intensities from each time exposure image across the chosen timescale, in this case two weeks, as shown in Fig. 8. For each x and y coordinate of the time exposure image ($\bar{I}$), the (mean) pixel intensity ($P$) is retrieved from that location; this is then repeated for each time exposure image, with the values being separated by $\Delta t$ — in this case either 30 or 60 min.

The resulting plot (Fig. 9d) shows the raw pixel intensities throughout a two week period, where periodic episodes of high and low intensities generally indicate tidal cycles of wetting and drying. The value of the radar pixel intensity at the peaks will not be regular as it is a function of local weather and surface conditions. These include wind speed (which roughens the sea surface), wave height and wave direction relative to the radar antenna location, which contribute to varied backscatter of radar energy from the sea surface.

The two week length of the analysis period was chosen to include a full spring–neap cycle, thus maximising the vertical intertidal range able to be detected by this method, whilst maintaining a reasonable temporal resolution through a year. It would be possible to reduce the analysis period to approximately a week and still maximise the intertidal range experienced at a site, provided the analysis period was precisely half the exact spring–neap cycle length and synchronised such that each analysis period covered either the interval from neap to spring or from spring to neap. Periods less than this could also be used, perhaps even a single tidal cycle, but there would be times when the analysis period would be focussed only on the smaller intertidal range at neaps, which does not make best use of this overall approach.

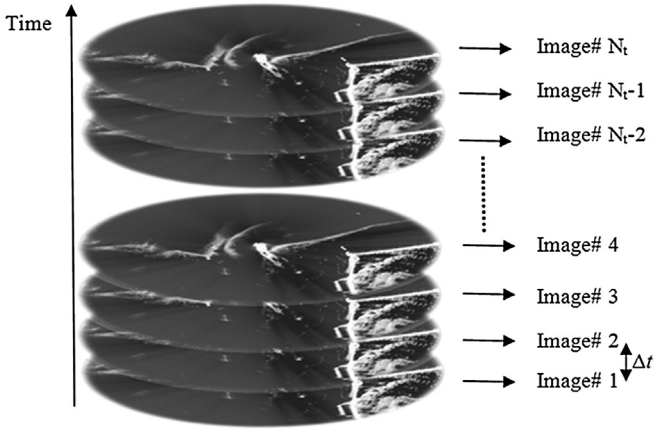


**Fig. 8.** Time-exposure image timestack used to form 3D matrix from which pixel intensities are extracted at each time step and location.

In order to relate the tidal variation in pixel intensity at a given location to an elevation, a set of water levels was chosen reflecting the potential tidal range of the deployment area; for Hilbre Island this was 0.5–10 m in 10 cm increments. For each of these elevations, the synthetic tidal record was used to determine whether a pixel at that elevation would be either covered by the tide, or exposed at the times corresponding to each radar record. This yielded a binary pulse sequence unique to each elevation, illustrated in Fig. 9b. Peaks in the absolute gradient of that binary pulse sequence (Fig. 9e) represent the points of transition between wet and dry at a given elevation.

The example pixel intensity time series shown in Fig. 9d is not a clean binary pulse sequence like the one generated by the tidal record in Fig. 9c, due to changing weather and surface conditions over the two week analysis period. Further, the presence of strong radar reflectors such as rocks in some pixels can exhibit a high radar cross-section that is then reduced by inundation with water, thus inverting the expected pulse sequence.

In order to allow a more like for like comparison between the binary sequences of Fig. 9c and the analogue time series in Fig. 9d, we attempt to normalise the analogue time series. The absolute gradient of the time series is calculated and the gradient peaks selected (representing sharp changes in intensity) using a robust peak-finding algorithm described by Yoder (2011); these peak values were then normalised and other non-peak values reduced to zero (Fig. 9f). Similarly, the absolute gradient is also taken of the binary wet–dry pulse sequences, illustrated in Fig. 9e.

It is then a straightforward matter to step through each possible elevation and determine a measure of similarity between the theoretical and measured pulse sequences. In this case we use the normalised cross-correlation to calculate R, the correlation coefficient at each elevation being:

$$R_N = \left\{ \frac{(P-\overline{P})(T_N-\overline{T}_N)}{\sigma_P\,\sigma_{TN}} \right\}. \quad (1)$$

The normalised correlation coefficient (R) for each water-level number (N) is calculated using Eq. (1), where P is the pixel intensity gradient record and T is the record of tidal state change gradients, $\sigma_P$ and $\sigma_T$ indicate the standard deviation of $P$ and $T$, respectively.

Each tidal elevation value now has a correlation coefficient (R) value defining the strength of the relationship between the record of pixel intensity gradients and the expected wetting and drying pattern at a given individual pixel location (Fig. 10). The maximum coefficient is used to indicate the tidal elevation of the waterline and the process is repeated for all pixel intensity records from every pixel location in the input image sequence. The results are then used to populate a matrix which builds up a map of intertidal pixel elevations above chart datum.

It can be seen from Fig. 9d and the derived pulse sequence in Fig. 9f that there are times when the transition between wet and dry is not evident in the data, probably due to very calm weather conditions. If one attempted to apply the conventional approach of identifying a physical waterline in the radar images from records around that time, it would not be possible because that information is not contained within the data. However, by taking the temporal approach to the problem, provided there are at least some measurable wet–dry transitions during the two-week time period, the absence of even days of wetting and drying transitions can be tolerated as can the occasional erroneous identification of a transition caused by heavy rain for example.

Pixel records from areas which are submerged even at low tide (subtidal areas) generally yield low correlation coefficients with the predicted wetting & drying pulse sequences. These areas are filtered out by setting a simple threshold in the correlation coefficient as a quality control. The resulting maps can be used to visualise the mean elevations over a single spring–neap cycle.

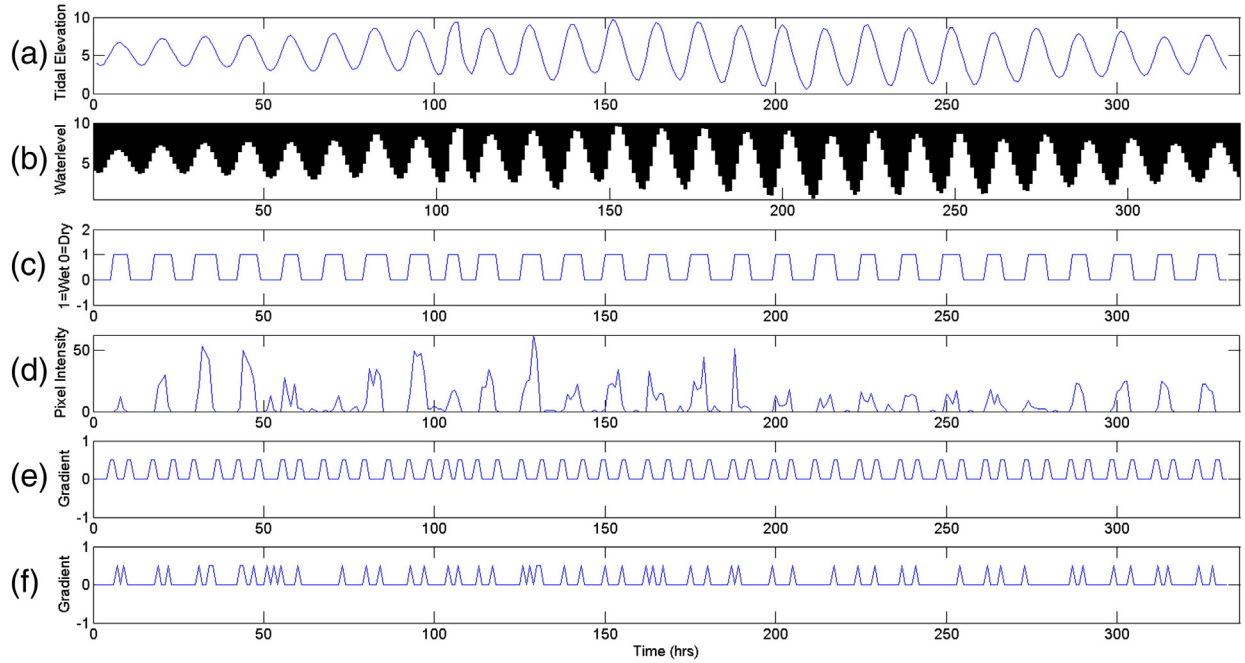


**Fig. 9.** (a) Tidal elevations over two weeks sampled concurrently with the radar time-exposure image; (b) matrix of binary wet–dry values based on tidal elevation; (c) example row extracted from b showing the tidal square wave indicating wet or dry at a water level of 5 m ACD; (d) raw pixel intensities over two weeks extracted from a single location; (e) absolute gradient of the tidal square wave showing transition times from wet to dry; (f) processed gradient of the raw pixel time series, approximating the transition times from wet to dry at a given location.

## 4. Results

The Temporal Waterline method described above was used to process radar data from March 2006–January 2007. For each two week period during that time, the analysis yielded both an elevation map corresponding to the wetting and drying transitions and also a corresponding correlation coefficient map reflecting the confidence level of the estimated elevations at each pixel location.

An example of a correlation map from April 2006 is shown in Fig. 11. Pixels with higher correlation values should provide a more reliable elevation estimate, whilst lower correlation points should potentially be removed as a quality control measure. Generally, the non-mobile areas generate very strong correlations, for example the rock armouring and sea wall of a recreational marine lake to the south-east is picked out clearly on the image with high correlation values of approximately 0.8, along with the well-established sandbanks and isolated rocks across the estuary. Lower correlation values of 0.3 or less are seen in the areas which are still submerged at low tide as these areas should not exhibit a tidal fluctuation that corresponds with wetting-and-drying.

Radar data collection is inhibited through shadowing, a phenomenon common in the analysis of ocean waves with low-grazing angle radar (Lynch and Wagner, 1970; Mattie and Harris, 1978). Even with the radar being sited on a tower, the large radial range over which data has been recorded means that some intertidal areas will still be shadowed from the radar signal, and these areas also exhibit low correlations. Clear, unobstructed line of sight to the intertidal area of interest

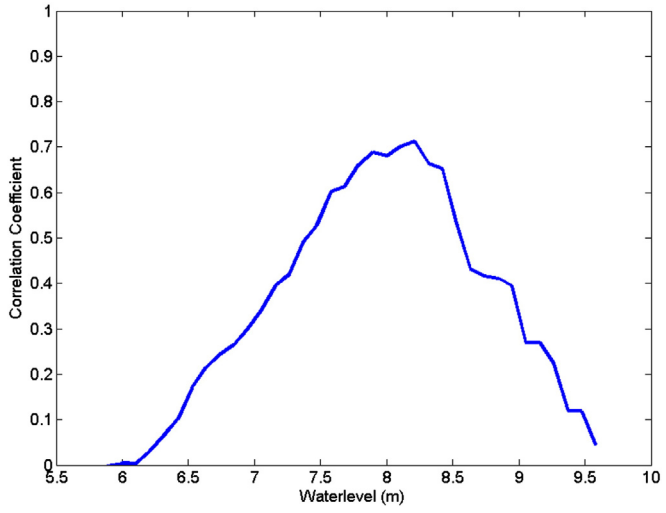


**Fig. 10.** Correlation coefficients for a given pixel record at water levels within the tidal range.

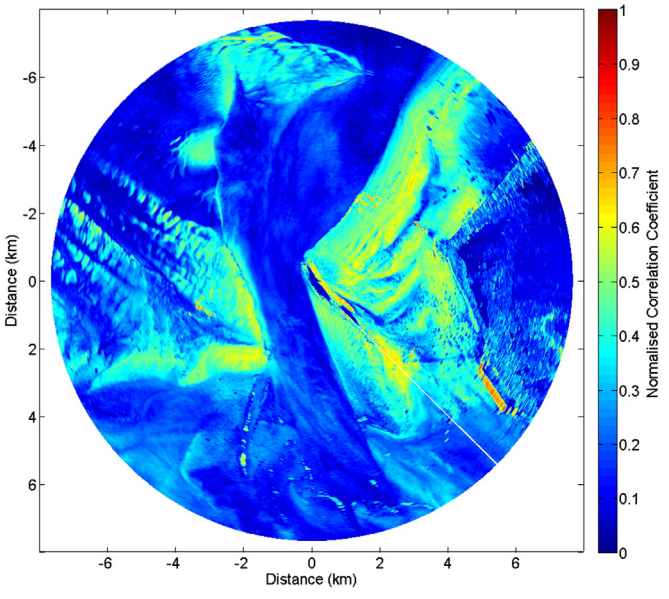


**Fig. 11.** Maximum correlation values at every location across the survey area. The correlation coefficient at each point has been matched to a specific tidal water elevation above chart datum. The strength indicates the confidence of the derived elevation.

is therefore an important consideration when selecting a deployment site. A subjectively chosen correlation threshold of 0.3 was used to filter out the values generally corresponding to subtidal and shadowed areas as a quality control process. Land areas and the islands have been masked out and set to an arbitrary elevation above the maximum tide.

A single waterline map is shown in Fig. 12 illustrating the mean intertidal bathymetry over a two-week period; successive analyses over a longer time period will be useful in isolating and monitoring the movement of bed features over different timescales. The intertidal sand flats of West and East Hoyle bank are clear in Fig. 12, as are the banks of the large central channel. This is one of two channels into the Dee estuary which connects to the canalised River Dee and the city of Chester 20 km higher up the estuary. A striking result is that the wreck of the Greek cargo ship SS Nestos displayed in Fig. 13, stranded and sunk on the sandbank in 1941, can be seen clearly to the north, with an elevation of ~3.5 m at low tide.

### 4.1. Temporal filtering and smoothing of elevation values

The elimination of pixels by any quality control process would lead to unwanted gaps in individual elevation maps. It would not be appropriate to spatially interpolate the missing values as the gradient of complex beach profiles is rarely linear and assuming such could lead to significant errors in further processing (Holman and Bowen, 1979).

However, the existence of multiple sequential records allows an alternative approach to be taken to mitigate and filter points with intermittent poor correlations. A weighted temporal smoothing of the time series of each pixel was applied to the ten months of results. The square of the correlation coefficients was used to weight each elevation at each two-week time step in a five point running smoothed fit using a robust smoothing algorithm by Garcia (2010). This has the effect of strongly smoothing the resulting time series of elevations whilst emphasising points with good correlations and de-emphasising those with weak correlations. An example of the results of smoothing the data in this way can be seen later in Fig. 16b.

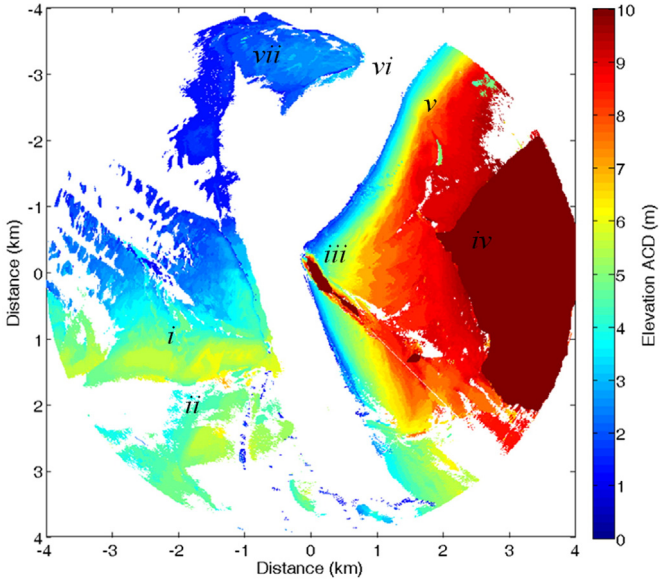


**Fig. 12.** Radar-derived elevations across the survey area showing beach profile and sandbanks in addition to the Hilbre channel and subtidal zone. Regions of interest include; (i) West Hoyle sandbanks; (ii) the Welshman's Gut (ephemeral channel linking the two main channels of the Dee estuary); (iii) Hilbre Island; (iv) the Wirral Peninsula; (v) East Hoyle bank; (vi) Hilbre swash; and (vii) sandbank with wrecked vessel (see Fig. 13).

### 4.2. Physical meaning of the waterline

The algorithm described here operates in the time domain rather than the spatial domain, hence it is not immediately obvious how the derived waterline relates to an individual record. Fig. 14 gives an example of how the derived waterline relates to both the LiDAR survey and the wave signatures on an individual radar record along a cross-shore transect. The record started at 06:00 on the 6th October 2006 and finished at around 06:10 after recording 256 images under relatively low wave conditions, just before a significant wave event. A cross-shore transect from the radar backscatter time series, and corresponding to transect 2 in Fig. 15, is shown in the plot as it progresses through just over 10 min of data. The left-hand side of the plot corresponds to the onshore (dry) sand flats whilst the right-hand side has the sea clutter of the waves approaching from right to left. The tidal elevations at the start, middle and end of the record were 2.97 m, 3.11 m and 3.29 m respectively. Fig. 14a shows how the radar backscatter profile evolves over the ten minutes. The wave breaker line is clearly evident around $x = 550$ m, and the change in water level on the location of the breaking waves on the beach profile is immediately evident, with the breaker line having moved approximately 25 m as the water level rose by over 30 cm during that time. Shoreward of the breaker line to the left, there are some strong backscatter targets that appear to move around, and inspection of the full radar image sequence verified that these are almost certainly sea birds moving around either singly or in groups on the sands. Fig. 14b shows the temporal mean of that backscatter profile. The cyan line marked on both plots indicates the location where the still water level with respect to the LiDAR survey in the middle (at 06:05 am) of the radar record would lie. The red, green and blue lines mark the corresponding derived average waterlines from the 2 week period ending on the 8th October 2006, and at the start, middle and end of the 06:00–06:10 6th October 2006 record respectively. The line corresponding to the middle of the radar record in time (green line) is close to the peak of the backscatter associated with the breaker line, which corresponds well with the peak of the breaker backscatter used as the criterion for defining the water line used by Takewaka (2005).

Since the waterline derived here relates to the peak in the shore breaker zone, it is slightly offshore of that which might be expected from the LiDAR elevation plus still water level at that time, which is the factor generating the slight overestimate in overall beach elevations described later.

### 4.3. Changes in beach transects

Fig. 15 shows the location of five cross-shore transects extracted from the processed dataset. These transects capture most of the foreshore beach extending from the subtidal boundary to the backshore where the gradient decreases. Transect 5 is the northernmost, with transect 1 being closest to the Island.

Fig. 16 shows the results of extracting these transects every two weeks from 10 months of data, each row represents elevations along the transect from on to offshore. Noisy data appear most prominently across all transects around time step 10 and 17 (29/07/2006 and 4/11/2006). This could be the result of very calm weather during the two-week sample periods, resulting in a smoother sea surface (i.e. less sea clutter) and lower correlation coefficients. The mean offshore significant wave heights for these time steps were 0.66 m and 0.82 m according to the CEFAS Wavenet buoy (WMO ID:62287) in Liverpool Bay compared to a mean of 0.92 m and a maximum of 4.89 m seen in January 2007 (these wave data are accessible from http://www.cefas.defra.gov.uk). Waves of this height (<1 m) are difficult to detect with marine radar (although the wave heights will have increased as the waves shoal), so it is unsurprising that the data are poor for these periods. From Fig. 15 it is clear that transect 5 runs close to a channel in the sand flats where shadowing inhibits the radar line of sight. Fig. 17 shows the start and end transects from the ten months of data, which

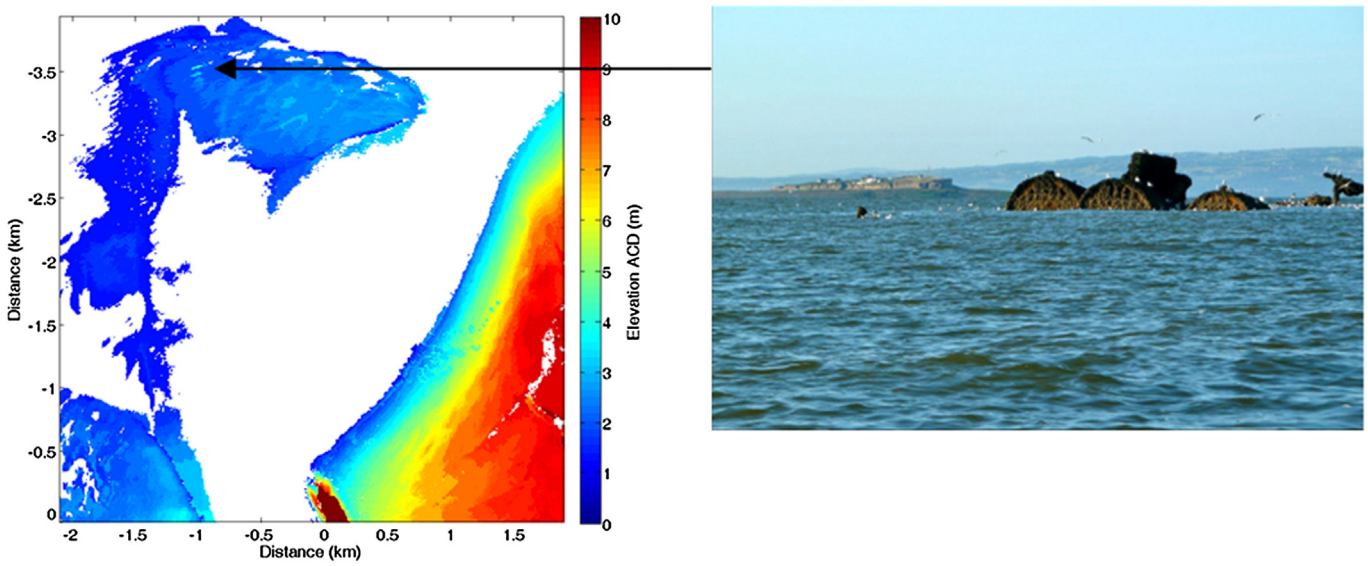


**Fig. 13.** Location of the wrecked cargo ship SS Nestos. Photo courtesy of John M.X. Hughes.

demonstrate that there is evidence of changes to the beach level during that time and that those changes in beach profile are quantifiable from the waterline derived topographic maps. Although there are small sections of the beach that move seawards and that appear to be associated with the crests of large bedforms, the overall pattern of change is a mean shorewards migration of the beach profile, which may be a seasonal effect rather than a long-term trend of erosion.

Table 1 lists the mean changes both in elevation along the transects and horizontally in terms of the cross shore translation of the beach profile from the beginning to the end of the ten-month period. Vertical elevation changes averaged over each profile range from an erosion of 0.05 m at the transect furthest from the radar to an erosion of 0.17 m at the transect nearest the radar. These are relatively small overall changes in bed level, but due to the shallow profile of the beach, these translate to considerable shorewards translation of the beach profile by between 25 m (furthest) and 40 m (nearest). The vertical variations are well within subjective observations by one of the authors of considerable variations in beach level relative to the rocks adjacent to Hilbre Island of significant fractions of a metre. Future work will use a larger 3-year dataset to investigate seasonal and inter-annual variations in

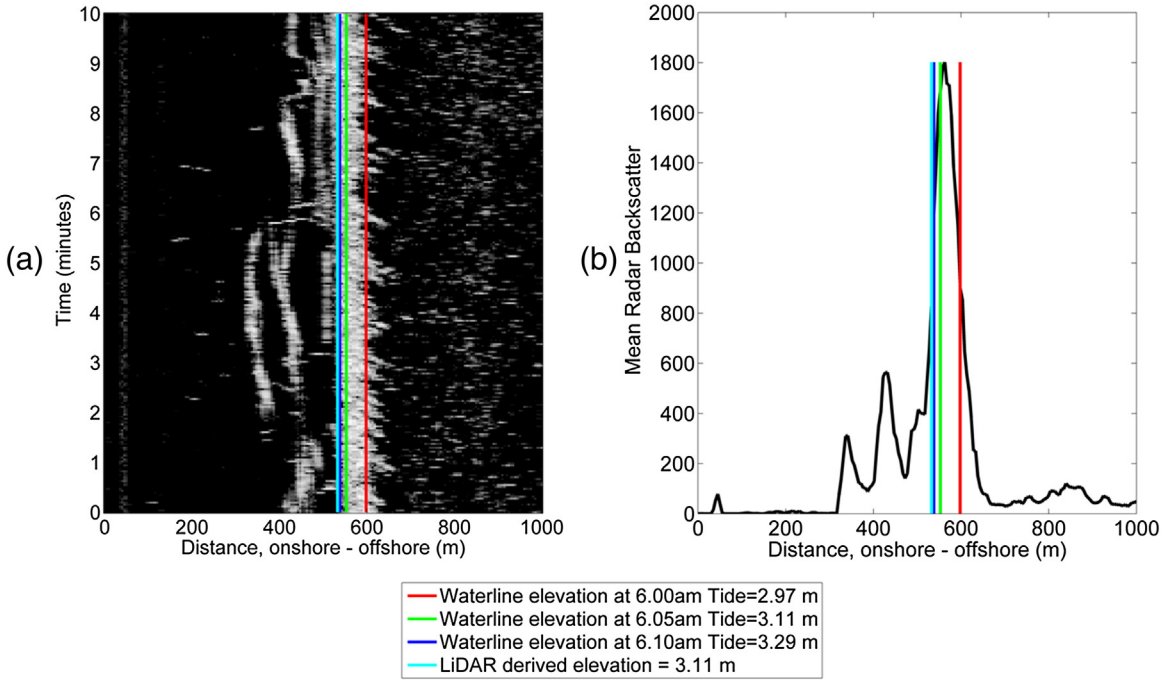


**Fig. 14.** (a) The evolution of a radar backscatter cross-shore profile over ten minutes for the record starting 06:00 6th October 2006, with the wave breaker line clearly evident around x = 550 m. (b) The temporal mean of that backscatter profile (uncalibrated intensity scale). The cyan line marked on both plots indicates the location of the still water level with respect to the LiDAR survey in the middle (at 06:05 am) of the radar record. The red, green and blue lines mark the corresponding derived average waterlines from the two week period ending on the 8th October 2006 at the start, middle and end of the record respectively. (For interpretation of the references to colour in this figure legend, the reader is referred to the web version of this article.)

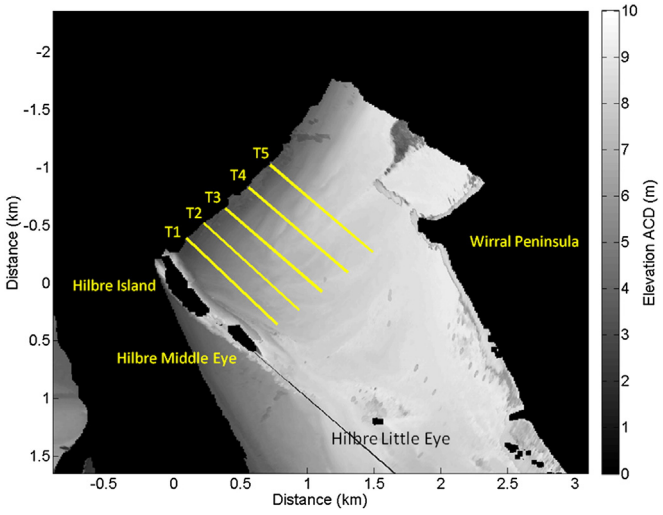


**Fig. 15.** Locations of cross-shore transects extracted and analysed over a ten month period.

the beach elevations and track large sandwaves/dunes as they evolve and migrate.

It is further noted that the changes in the transects over time strongly suggest the presence of migrating intertidal sand bars or waves, the dimensions and movements of which could be quantified with this technique. Studies by McCann (2007) and Way (2013) have previously documented the length and migration rates of these sedimentary bedforms but the profiles could not be remotely determined with the earlier approach. These features have wavelengths of the order of 100 m–200 m and have been observed to migrate in excess of 100 m per year landwards using the radar signatures of breaking waves over the waves as a proxy indicator for their position. It is hoped that the ability to measure sediment volume changes cost effectively over long time periods will allow variations in sediment fluxes within the surveyed area to be quantified effectively. This idea will be explored in further work.

### 4.4. Fixed elevation control points

The changes observed in these transects demonstrate that the method is capable of determining surprisingly small changes in beach elevations provided the changes are real and not artefacts of seasonal changes in wave height. To investigate this possibility, a number of rocky outcrops in the intertidal zone were chosen as control points that should not vary in elevation. If the results showed that these targets did not vary in elevation through the ten months of the study period, then it would be reasonable to assume that changes in the elevations of potentially mobile sandy areas nearby during the same period are genuine.

The locations of these control points are shown in Fig. 18. One site is located on Hilbre Island itself, another on a rock platform close to the Island, one from Hilbre Middle Eye, and the final site is from the rock armour protecting the recreational marine lake at West Kirby.

The time series of waterline-derived elevations for each control point are displayed, with waterline elevation relative to Admiralty Chart Datum (m) on the y axis and time in two-week intervals along the x axis. The plots show that radar-derived elevations at these control points are relatively stable across 10 months, and thus it is concluded that the elevation changes observed in the sandy areas are almost certainly genuine.

### 4.5. Relationship between the waterline elevation and the absolute intertidal elevation

It should be emphasised that the elevations determined by this method are those of the waterline relative to the tidal water level. This is not the same as the absolute elevation that might be surveyed by LiDAR or other survey methods. However, the purpose of beach transects and surveys themselves should be considered before a discussion

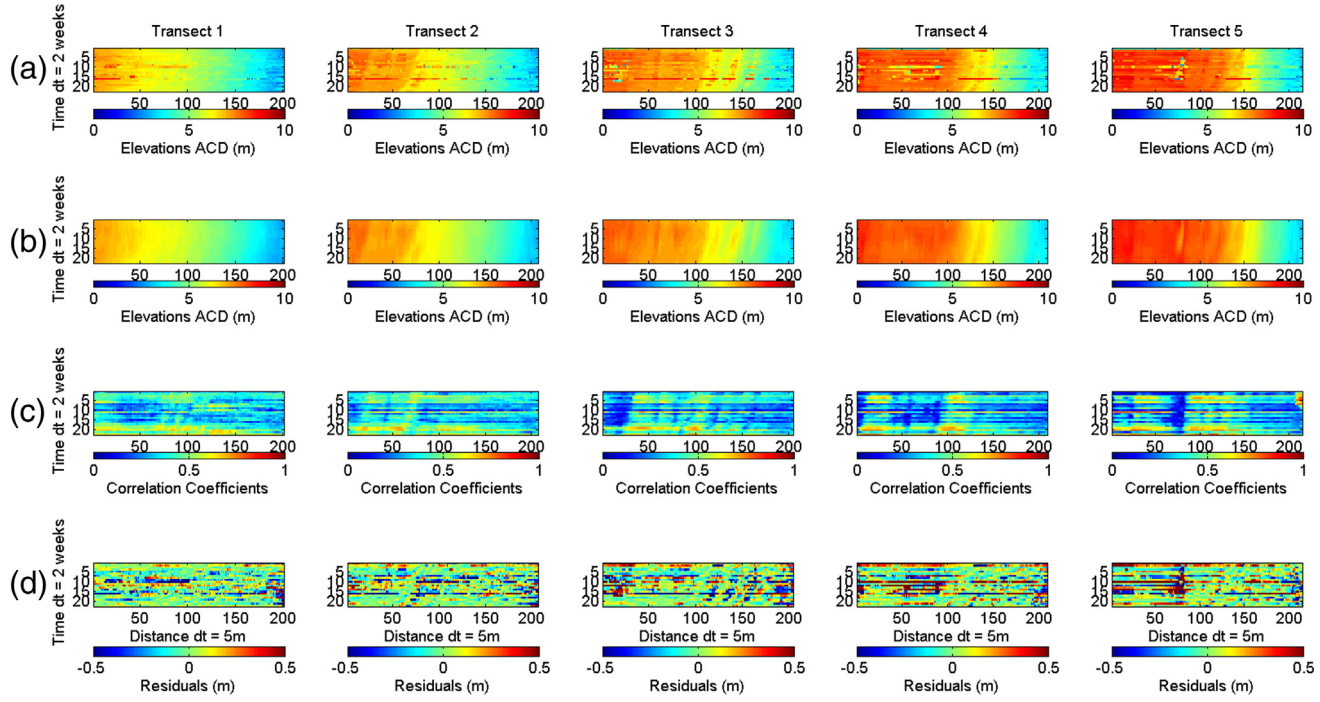


**Fig. 16.** (a) Raw radar-derived elevations extracted along each cross-shore transect through time. Each row shows mean elevations over a two-week period; (b) elevation transects from the same locations taken from data smoothed using a weighted linear filter; (c) correlation coefficients at each point along extracted transects; and (d) differences between raw data and the filtered data, ensuring the introduction of smoothing artefacts is minimal.

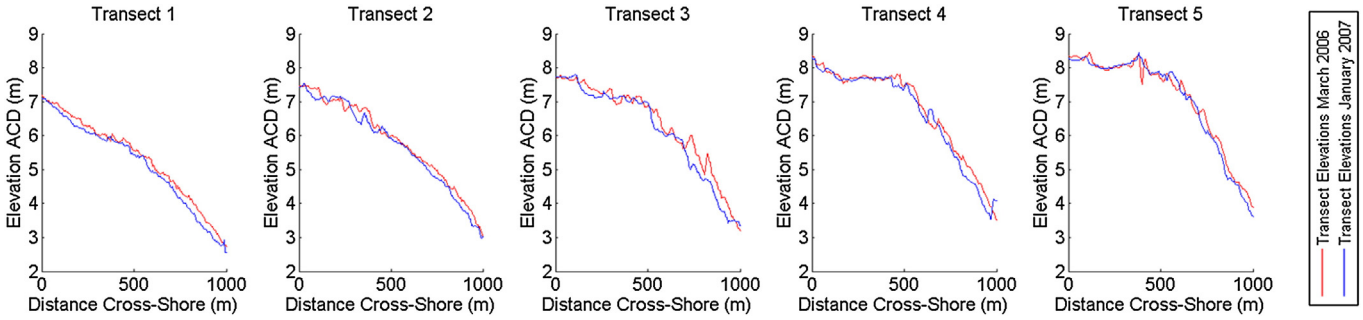


**Fig. 17.** Waterline transects at the start (red) and end (blue) of the ten month study period. All transects show overall erosion and setback of the beach foreshore. (For interpretation of the references to colour in this figure legend, the reader is referred to the web version of this article.)

of relative accuracies of one method against another. The purpose of many beach transect monitoring campaigns is to determine to what position the combination of waves and tides might reach, damage sea defences and potentially overtop beaches and sea walls. Conventional surveys are carried out to absolute elevation datums, then tidal elevations can be combined with models of wave setup and runup to estimate how high up the beach the water would reach under various conditions. Waterline methods potentially supply this information directly, without the need for the modelling step, so absolute accuracy of the waterline derived elevations relative to a survey may be less important than the long term stability of the technique.

Fig. 19a shows the elevations determined by the Temporal Waterline method cropped to the areas covered by the October 2006 LiDAR survey. Fig. 19b shows the LiDAR survey itself. The general shape, location and elevations of the coastline and sandbanks detected by the waterline method are mostly in good agreement with the LiDAR survey. There is an area of particularly poor results to the southwest of the study area in Fig. 19a where the radar method overestimates bed elevation by an excess of 5 m in places. These areas were therefore removed in order to prevent contamination of further analysis. A combination of the shadowing effect of the sandbanks at mid- to low tide and the increasing lack of sea clutter at locations further into the sheltered estuary is thought to be the cause of the concentrated area of poor results. It is, however, significant that the present processing and filtering techniques do not remove these poor elevations and the pixel records in these areas often have seemingly valid matches with a given tidal elevation. Identifying the reason for this and addressing the issue is a priority for future work.

In order to quantify the differences between the LiDAR and radar elevation plots, the LiDAR values at each point were subtracted from the radar-derived values. Fig. 20 shows these residuals. The majority of the radar-derived elevations lie within±1 m of the corresponding LiDAR elevations, with the overall pattern indicating that the waterline-derived elevations are slightly higher than the survey elevations. Intuitively this might be expected due to contributions from wave setup and runup. However, the steeper beachfaces within 2 km of the island show surprisingly good agreement with the LiDAR survey, which may indicate that the wave runup and setup may not be the only factors involved in the differences.

Consistent differences between survey and waterline elevations with strong correlation values are evident over the flatter areas of the sand banks. This suggests there may be additional effects that add to the elevation of the water, such as pooling of the water between sediment features.

Fig. 21 shows a comparison between the waterline derived elevations and the corresponding LiDAR transects. These reveal that the sloping parts of the transects leading down to the low water mark are relatively well matched between LiDAR and waterline. However, the flatter areas bounded by sediment bars or sandwaves appear to have water trapped behind the bedforms, supporting the idea that water is pooling on the sand flats and creating some of the differences between LiDAR and waterline maps. As has already been noted, the reflectivity data associated with the LiDAR elevations also indicated pooling of water in these areas, even at low water.

This is an effect known to exist by the authors, based on numerous trips walking to the island. As the tide goes out, it takes a considerable time for the water to drain off the flatter areas, and it is often advisable to wait an hour or two beyond the time when the tide has nominally gone out to allow sufficient water to drain off the sand flats before setting off for the island on foot.

These factors indicate that the simplification of applying the water level associated with the tide gauge location on Hilbre Island across the whole domain is probably an over-simplification.

### 4.6. Close-range (<3 km range) accuracy

In order to better compare the features present in the LiDAR and radar-derived elevations and the spatial distribution of differences at the closer range, Fig. 22 shows a subsection of the data covering the area of the northeastern beach in more detail. Fig. 22(a) shows the radar derived waterline results; (b) shows the LiDAR survey; (c) the difference between the waterline and LiDAR elevations and (d) the areas likely to be shadowed based on ray tracing and the LiDAR survey. It is clear from the difference plot in Fig. 22(c) that the waterline method determines absolute elevations along the immediate eastern and southern beach very well. Areas further from the radar and thus also further from the location relating to the water level data show an increasing over estimate in the elevations compared with the LiDAR survey. Some areas of the sand flats are shadowed from the radar, as illustrated by the shadow plot in Fig. 22d, calculated from the LiDAR survey using a simple ray-tracing approach. Thus elevations calculated for these areas are not likely to be accurate.

Fig. 23 shows a series of error histograms comparing the LiDAR elevations with those of the Temporal Waterline at different ranges from the radar. The region within 0.75 km of the radar location (Fig. 23a) exhibits a mean bias of 0.12 m higher than the LiDAR survey, whilst the regions from 0.75 km–1.5 km (Fig. 23b); from 1.5 km–2.25 km (Fig. 23c) and from 2.25 km–3 km range (Fig. 23d) exhibit a greater bias of 0.52 m,

**Table 1**
Mean beach profile changes for profiles 1–5 in terms of elevation and cross shore horizontal translation. All transects show a small (<0.2 m) mean reduction in elevation over ten months, with corresponding mean values for the cross shore translation of the beach profile that are large due to the shallow (approximately 1 in 250) nature of the beach gradient.

| Transect | Mean vertical change (m) from March 2006 to January 2007 | Mean horizontal change (m) |
|---|---|---|
| 1 (Nearest to radar) | −0.17 | −37.7 |
| 2 | −0.10 | −30.3 |
| 3 | −0.16 | −39.6 |
| 4 | −0.10 | −30.8 |
| 5 (Furthest from radar) | −0.05 | −24.9 |

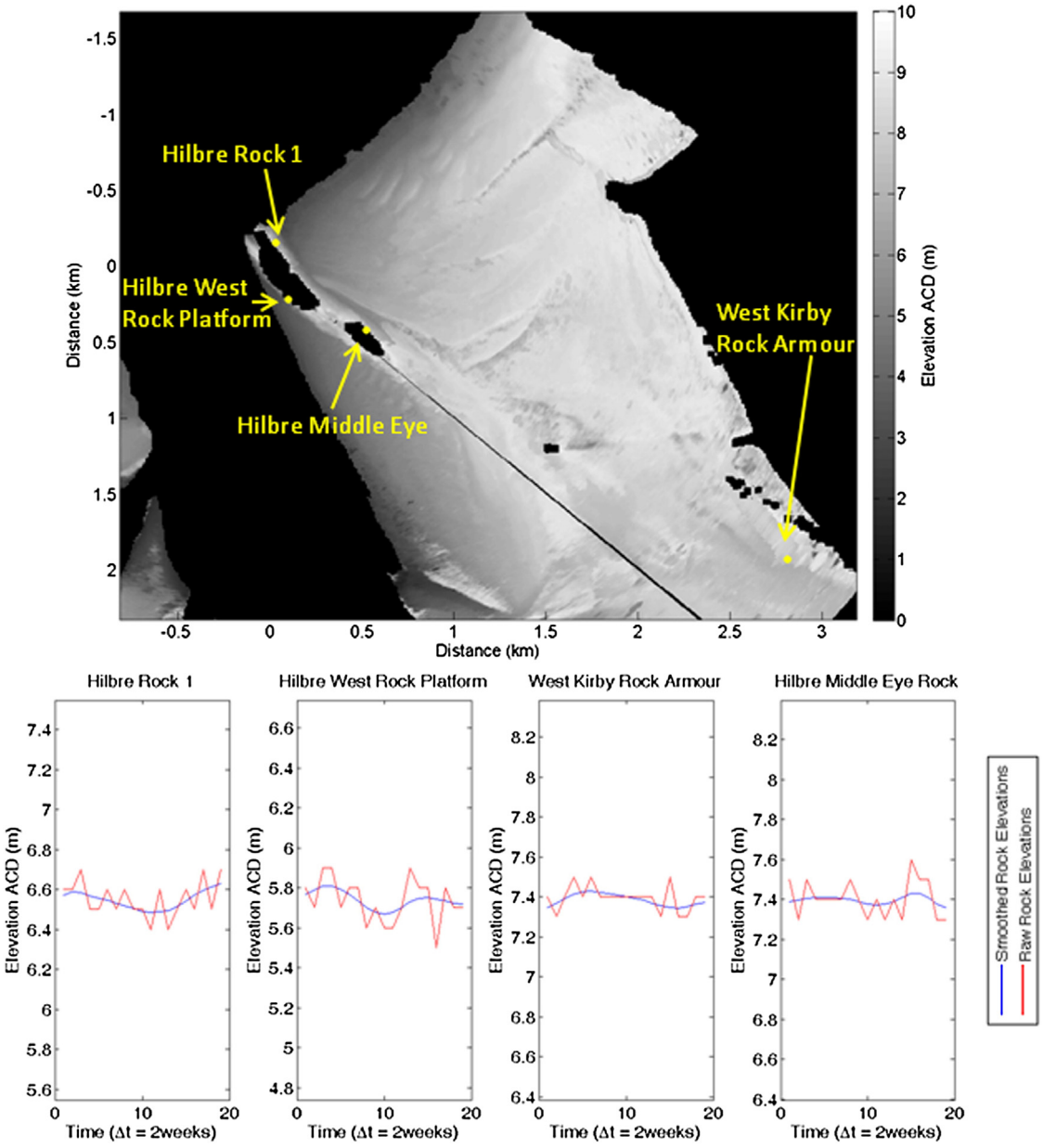


**Fig. 18.** Locations of rock control points and resulting elevations throughout the ten month analysis period, elevation records from the four sites, along with both raw (red) and smoothed (blue) elevations from each rock location. (For interpretation of the references to colour in this figure legend, the reader is referred to the web version of this article.)

0.48 m and 0.59 m respectively. These regions encompass more of the flatter areas of sand flats. This reinforces the conclusions from Fig. 21 suggesting these flatter areas consistently experience pooling water, and also include larger areas shadowed from the view of the radar which are likley to have erroneous values.

Further errors might be expected due to the simplification that the tidal elevation relating to the location of the Hilbre Island tide gauge defines the water level across the entire analysis area. The true pattern of water elevation across this complex macro-tidal environment must be expected to degrade with range from the measurement location. Moore et al. (2009), explored the differences in tidal asymmetry across the estuary via a numerical modelling study, showing stronger asymmetry over the sand banks compared with the channels, which confirms that our assumption of a uniform tidal elevation across the site at any particular moment is almost certainly an over-simplification. Attempts to apply a more realistic 2-D tidal elevation pattern either using a tidal propagation model or empirically may be explored in future work. In particular, the issue of pooling water taking time to drain off the sand flats might suggest that although the transition time of the rising tide may be relatively accurate across the study site, that of the falling tide may be delayed relative to the tide gauge location.

Some differences between the radar-derived elevations and the survey are also to be expected due to the different temporal scales of the two surveys. LiDAR is a near instantaneous snapshot in time whereas radar-derived elevations represent the mean conditions over a two week period in this case. Thus numerical comparisons must be considered in this light and a perfect match should not be expected. Significant changes to the shape and location of the sedimentary features have been observed to occur overnight by the authors, so the superficial features of the intertidal sand flats must be assumed to be varying slightly even from tide to tide under dynamic conditions. Such observations reinforce the value of what could be considered a more representative average measure of intertidal elevations than the snapshots provided by surveys such as LiDAR.

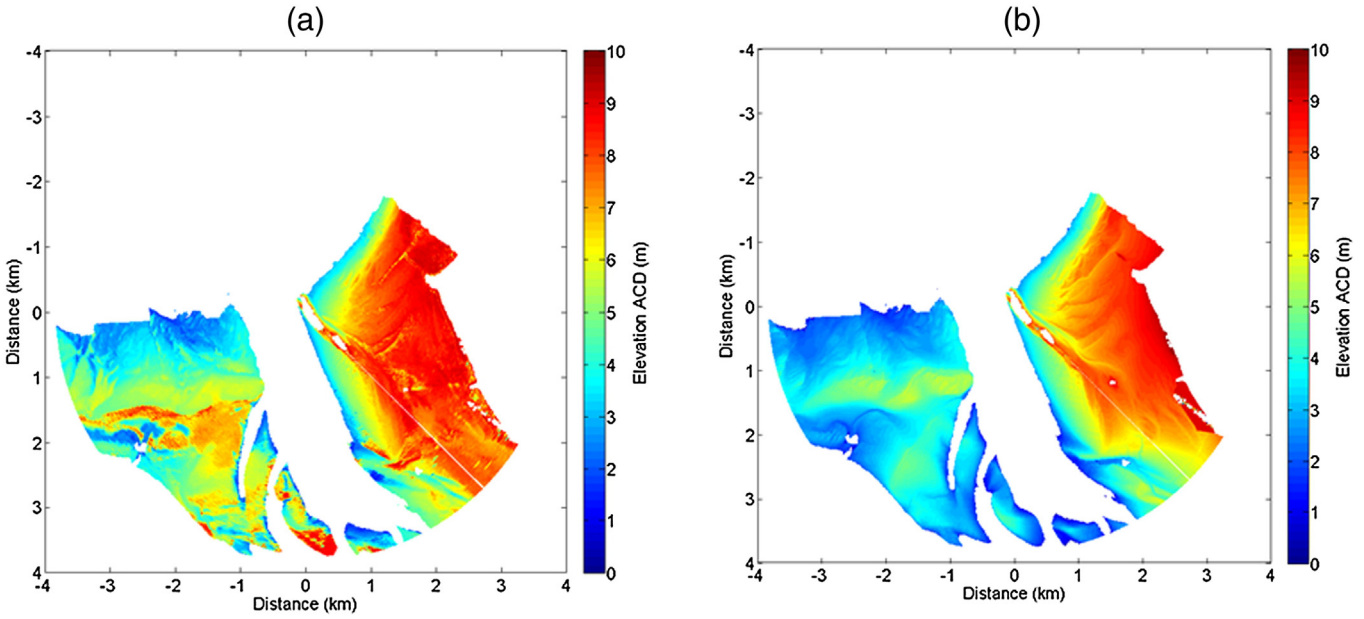


**Fig. 19.** Radar-derived (a) and LiDAR (b) elevations in October 2006.

### 4.7. Cumulative changes in elevation

Fig. 24 shows the cumulative variations in radar-derived waterline elevations at each point in the sand flat region of the domain over the course of 10 months, the green areas showing a high degree of stability. The most stable areas located around the landmass of Hilbre Island and the Peninsula represent concentrations of rocks. In addition, large swathes of the beach are clearly stable, suggesting a lack of medium-term sediment mobility over those regions. Regions with higher values of maximum difference in elevation through time are indicative of erosion or deposition. For example, the linear features seen across the beach face potentially mark out the migration of sand bar features, whilst areas of high change that are less linear may highlight areas subject to spatially discrete erosion or accretion. Overall, the plot illustrates that the majority of the area exhibits relatively little change over ten months, with isolated areas of mobile features representing largely superficial changes to that part of the estuary.

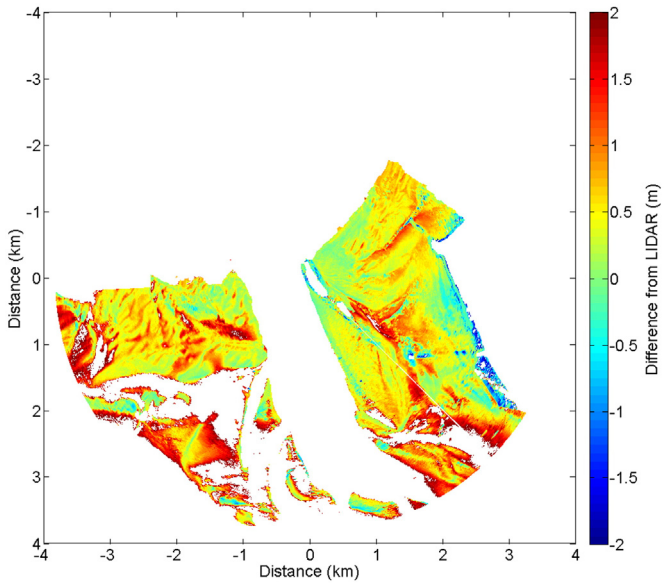


**Fig. 20.** Residuals between LiDAR and radar derived elevations.

## 5. Discussion

This new method of deriving maps of the intertidal zone, although relatively effective and simple in concept, relies on a number of assumptions that are probably over-simplifications at present.

The use of a single instantaneous tidal elevation across a complex estuarine environment is acknowledged by the authors to be a simplification of reality, and appropriate tidal propagation models may in future provide a more realistic spatially varying water level distribution across large areas. In particular, increasing tidal asymmetry across the sand flats and sand banks may be adversely affecting results in this complex area as a result of this assumption.

The present study was conducted in a macro-tidal estuary, in which there are extensive intertidal areas. At sites where a more modest intertidal zone is expected, consideration must be given to the expected width of the intertidal zone relative to the radar pixel size. If the intertidal beach width is narrow relative to the radar pixel size of 5–10 m, then X-band radar may not possess the appropriate horizontal resolution for the task. Instead, millimetre wave radar such as the 77 GHz version used by Bell et al. (2006) may be more appropriate as such systems are capable of sub-metre range resolution and have been demonstrated to respond well to the breaking waves and beach run-up that categorises the water line. Optical camera systems are also likely to work well with this technique and can provide similar sub-metre resolution within a reasonable range of the camera, albeit in daylight and good visibility.

Further, if the vertical tidal range is narrow, the elevation intervals used in the analysis could be made finer than the 0.1 m intervals used here. Even in micro-tidal areas, meteorological effects can introduce significant water level changes in excess of the astronomical tides, and the additional contribution of these would undoubtedly assist the success of the technique at such sites.

The accuracy of the method at the limits of the tidal range also requires further consideration. This is because the number of waterline transitions close to the water level limits of the spring–neap cycle will reduce, from the peak of a uniform two transitions per tidal cycle, i.e. over 50 transitions in 14 days, down to single figures and then none as the water level approaches and goes beyond the limits. Looking for

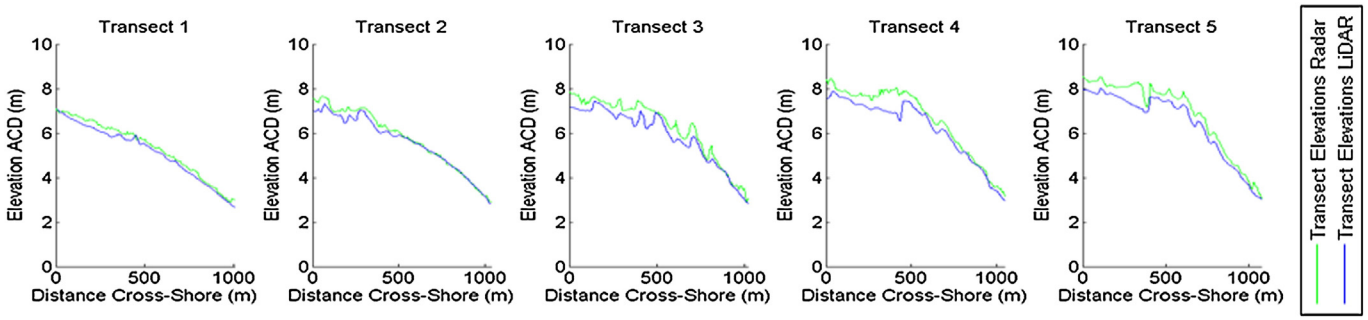


**Fig. 21.** Elevations along each transect from Fig. 15 with smoothed radar–derived (green) and LiDAR (blue) elevations. (For interpretation of the references to colour in this figure legend, the reader is referred to the web version of this article.)

a correlation between the radar-derived signatures and a tidally derived signal with only a few transitions will inevitably result in a less reliable match, and it would be prudent to implement a threshold in the number of wet–dry transitions below which any derived elevations are considered at least suspect if not invalid, regardless of the quality of the numerical match achieved. It may be that the mean low water and mean high water levels would provide standardised thresholds for this application in the future.

The temporal update rate was set to two-week intervals corresponding to a single spring–neap cycle and chosen to maximise the tidal range during each temporal analysis window. Further work may investigate reducing this interval to approximately a week or even less but should be synchronised to span neaps to springs or springs to neaps to ensure the maximum tidal ranges are experienced during each analysis period.

## 6. Conclusions

A new method of analysing the location of waterlines in remotely sensed data has been presented. The method differs from established methods by moving the problem from the spatial domain to the time domain and looking for matches in the expected temporal pattern of transitions between wet and dry areas over a spring–neap cycle. This is inherently more robust and easier to implement automatically than attempting to identify the precise physical waterline in individual remotely sensed images. The accuracy relative to a LiDAR survey varies from an over-estimate of 0.12 m within the first 0.75 km from the radar, to an approximately 0.5 m over-estimate further from the radar, although these comparisons are complicated by the complex nature of the macrotidal estuary used as the test case.

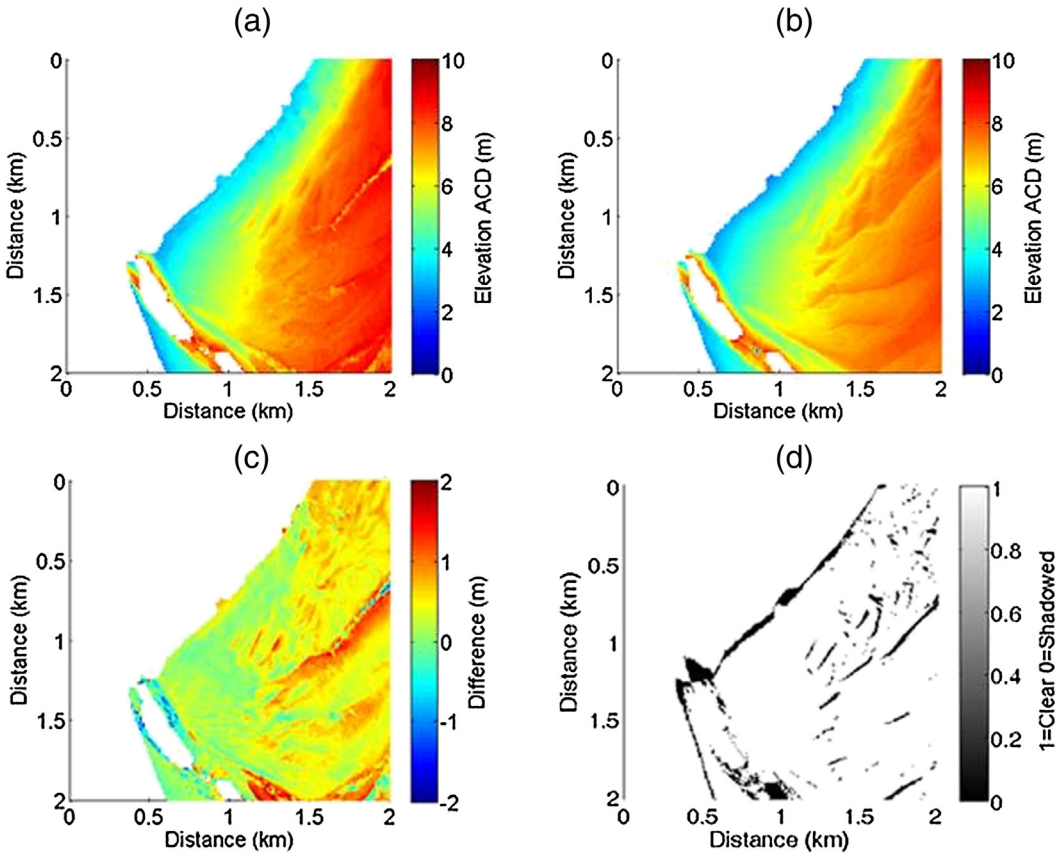


**Fig. 22.** (a) Extracted subsection of radar-derived; (b) LiDAR elevations; (c) the residuals between radar-derived and LiDAR elevation data; (d) an artificial line of sight shadow map, illustrating the radar line of sight based on the LiDAR observations, constructed using a simple ray tracing algorithm.

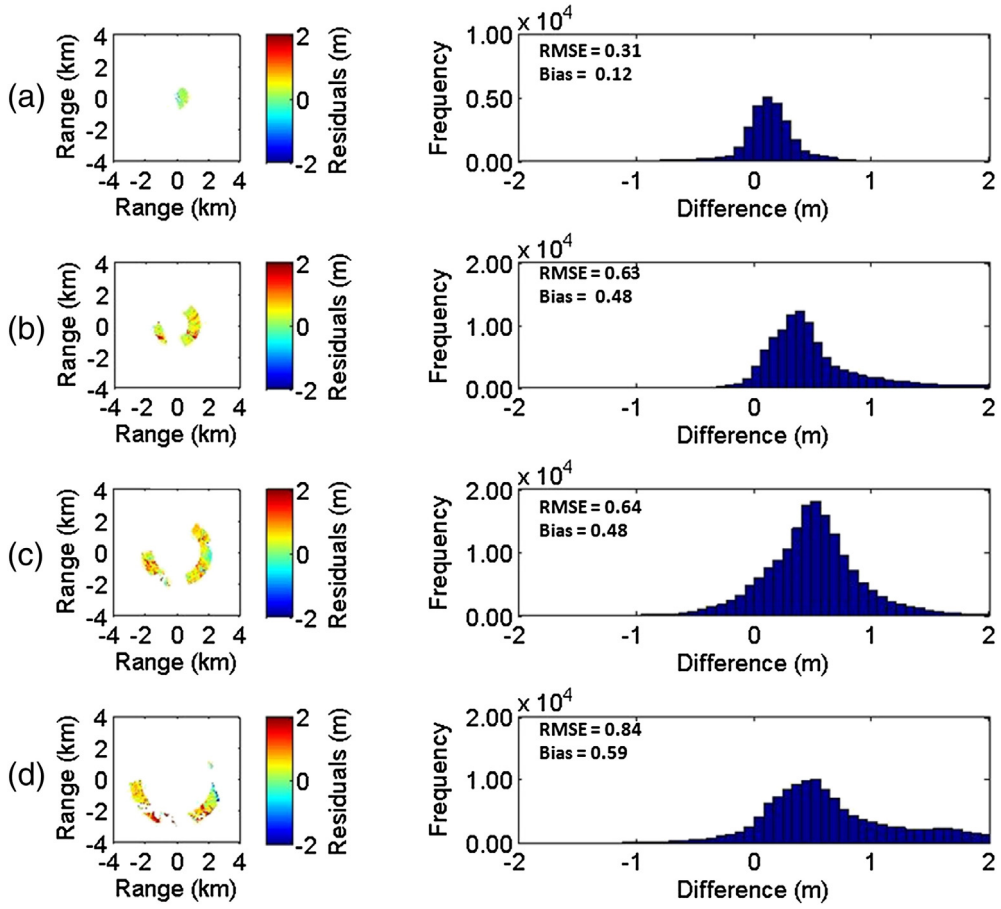


**Fig. 23.** Differences between the LiDAR and radar-derived waterline elevations at different ranges from the radar (left) and corresponding error histograms (right): (a) the region within 0.75 km of the radar location; (b) the region from 0.75 km range to 1.5 km range; (c) the region from 1.5 km–2.25 km; and (d) the region from 2.25 km–3 km.

The tidal water level used for the analysis is assumed to be flat across the study area at any instant in time, which is almost certainly an over-simplification, and the application of a modelled 2-D water level that took into account the tidal asymmetry over sand flats and sand banks may improve the absolute accuracy in future.

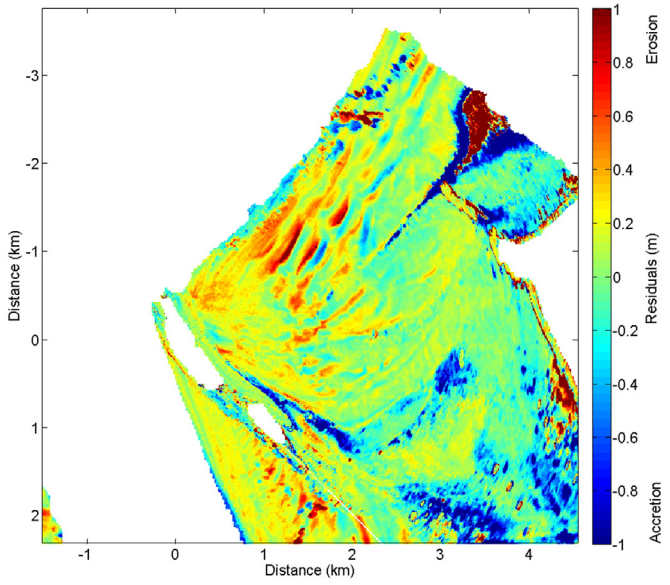


**Fig. 24.** Changes in waterline elevation from March 2006 to January 2007. Red indicates erosion whilst blue indicates accretion.

The method provides a map of the elevation of the waterlines relative to the tidal reference, rather than the absolute elevation of the bed. The analysis of pixels corresponding to a number of rocks demonstrated that elevations of the derived waterlines relating to those rocks are relatively stable through in 10 months of processed data. In contrast, inspection of a number of beach transects showed gradual evolution of those transects during the study period, with all beach transects exhibiting a slight lowering of the beach face during the 10 months from March 2006 to January 2007. Hence, the waterline elevations can be viewed as a very effective measure of intertidal change yielding volumetric changes that could be used in conjunction with a single validation survey to relate such changes to absolute elevations if necessary.

Despite these simplifications, the results are remarkably stable through time, suggesting that the method would be suitable for the autonomous monitoring of changes to large intertidal areas over sustained periods of months to years.

In commercial operation, the results from this method could be coupled with bathymetric survey data of navigation channels to create an integrated chart system, which would populate sub-tidal areas using data from conventional survey methods, and intertidal zones with waterline derived information. This would potentially provide regularly updated reports on sediment flux and channel migration. That said, the waterline method is effective as a stand-alone tool for monitoring changes in the intertidal channel margins. This combined mapping strategy may be a vital source of data for coastal stakeholders and port authorities operating in areas where sedimentary features are mobile across the intertidal area and those where sediment accretion or erosion

in between cycles of commissioned surveys and maintenance is causing problems in the management of the coast.

## Acknowledgements

The authors would like to thank Wirral Borough Council's Ranger Service and in particular the (then) Hilbre Island Ranger — Mr David Cavanagh, for many years of enthusiastic help with numerous aspects of installing and maintaining a remote system in such a challenging location. Thanks are due to Mr John M. X. Hughes for the photograph of the SS. Nestos exposed at low tide used in Fig. 13 and a set of insightful pilotage notes for the Dee Estuary. The radar data were collected by the *National Oceanography Centre (NOC) Liverpool* under the umbrella of the *Liverpool Bay Coastal Observatory* and was funded by the *UK Natural Environment Research Council under National Capability Funding. The authors also acknowledge Engineering and Physical Sciences Research Council funding for investigator time on the ARCoES project EP/I035390/1*. Cai Bird's PhD study was funded by the Centre for Global Eco-Innovation (CGE) through the European Regional Development Fund (ERDF) (X02646PR) and Marlan Maritime Technologies. The authors would also like to thank the anonymous reviewers, whose comments were extremely helpful in improving the content of this paper.

## References

Aarninkhof, S.G., Turner, I.L., Dronkers, T.D., Caljouw, M., Nipius, L., 2003. A video-based technique for mapping intertidal beach bathymetry. Coast. Eng. 49 (4), 275–289. http://dx.doi.org/10.1016/S0378-3839(03)00064-4.

Aarninkhof, S.G.J., Ruessink, B.G., Roelvink, J.A., 2005. Nearshore subtidal bathymetry from time-exposure video images. J. Geophys. Res. 110 (C06011). http://dx.doi.org/10.1029/2004JC002791.

Annan, J., 2001. Hindcasting coastal sea levels in Morecambe Bay. Estuar. Coast. Shelf Sci. 53, 459–466. http://dx.doi.org/10.1006/ecss.1999.0626.

Austin, M.J., Masselink, G., 2006. Observations of morphological change and sediment transport on a steep gravel beach. Mar. Geol. 229 (1), 59–77. http://dx.doi.org/10.1016/j.margeo.2006.02.003.

Bacon, Sir R., 1932. The concise story of the Dover Patrol. Hutchinson & CO. LTD., London, UK.

Bailey, M., 2009. Report on the state of the navigation of the River Mersey. Department for Transport. Mersey conservancy. Port of Liverpool. Available at:, http://assets.dft.gov.uk/publications/report-on-navigation-of-river-mersey-2009/report.pdf (Date accessed: 08/08/14).

Bell, P.S., 1999. Shallow water bathymetry derived from an analysis of X-band marine radar images of waves. Coast. Eng. 37, 513–527. http://dx.doi.org/10.1016/S0378-3839(99)00041-1.

Bell, P.S., 2008. Mapping shallow water coastal areas using a standard marine X-band radar. Hydro8, Liverpool, 4th-6th November. 2008. Liverpool, International Federation of Hydrographic Societies.

Bell, P.S., Inventor; Natural Environment Research Council, assignee. 2014, march 3rd. Inter-tidal mapping. International Patent Application No. PCT/GB2014/050908.

Bell, P.S., Osler, J.C., 2011. Mapping bathymetry using X-band marine radar data recorded from a moving vessel. Ocean Dyn. 61, 2141–2156. http://dx.doi.org/10.1007/s10236-011-0478-4.

Bell, P.S., Williams, J., Clark, S., 2006. Nested radar systems for remote coastal observations. In: Proceedings 8th International Coastal Symposium (ICS 2004). J. Coast. Res. Spec. Issue 39, pp. 483–487.

Bell, P.S., Lawrence, J., Norris, J., 2012. Determining currents from marine radar data in an extreme current environment at a tidal energy test site. Geoscience and Remote Sensing Symposium (IGARSS)2012 IEEE International Conference. Munich pp. 22–25. http://dx.doi.org/10.1109/IGARSS.2012.6351856.

Coakley, D.B., Haldeman, P.M., Morgan, D.G., Nicolas, K.R., Penndorf, D.R., Wetzel, L.B., Weller, C.S., 2001. Electromagnetic scattering from large steady breaking waves. Exp. Fluids 30 (5), 479–487. http://dx.doi.org/10.1007/s003480000220.

Dankert, H., Horstmann, J., 2007. A marine-radar wind sensor. J. Atmos. Ocean. Technol. 34 (3), 1629–1642. http://dx.doi.org/10.1175/JTECH2083.1.

Davidson, M., Van Koningsveld, M., de Kruif, A., Rawson, J., Holman, R., Lamberti, A., Medina, R., Kroon, A., Aarninkhof, S., 2007. The CoastView project: developing video-derived Coastal State Indicators in support of coastal zone management. Coast. Eng. 54 (6–7), 463–475. http://dx.doi.org/10.1016/j.coastaleng.2007.01.007.

De Vriend, H.J., Wang, Z.B., Ysebaert, T., Herman, P.M.J., Ding, P., 2011. Eco-morphological problems in the Yangtze Estuary and the Western Scheldt. Wetlands 31, 1033–1042. http://dx.doi.org/10.1007/s13157-011-0239-7.

Diop, S., Barusseau, J.-P., Descamps, C., 2014. The land/ocean interaction in the coastal zone of West and Central Africa. Springer, New York http://dx.doi.org/10.1007/978-3-319-06388-1.

Fernandes, R., Vinzon, S., de Oliveira, F., 2007. Navigation at the Amazon River mouth: sand bank migration and depth surveying. Ports http://dx.doi.org/10.1061/40834(238)52.

Fisher, J.S., Stauble, D.K., 1977. Impact of Hurricane Belle on Assateague Island washover. Geology 5 (12), 765–768. http://dx.doi.org/10.1130/0091-7613(1977)5<765:IOHBOA>2.0.CO;2.

Fitzgerald, D.M., Heteren, S. Van, Montello, T.M., 1994. Shoreline processes and damage resulting from the Halloween Eve storm of 1991 along the North and South Shores of Massachusetts Bay. U.S.A. J. Coast. Res. 10 (1), 113–132. http://www.jstor.org.

FitzGerald, D., Kraus, N., Hands, E., 2000. Natural mechanisms of sediment bypassing at tidal inlets. U.S. Army Corps of Engineers. Coastal Engineering Technical Note CHETN-IV-30. U.S. Army Engineer Research and Development Center, Coastal and Hydraulics Laboratory. Vicksburg, MS, pp. 1–10.

Flampouris, S., Seemann, J., Ziemer, F., 2009. Sharing our experience using wave theories inversion for the determination of the local depth. OCEANS. 2009-Europe Bremen http://dx.doi.org/10.1109/OCEANSE.2009.5278331.

Fuchs, J., Regas, D., Waseda, T., Welch, S., Tulin, M.P., 1999. Correlation of hydrodynamic features with LGA radar backscatter from breaking waves. IEEE Trans. Geosci. Remote Sens. 37 (5), 2442–2460. http://dx.doi.org/10.1109/36.789641.

Gao, J., 2009. Bathymetric mapping by means of remote sensing: methods, accuracy and limitations. Prog. Phys. Geogr. 33 (1), 103–116. http://dx.doi.org/10.1177/0309133309105657.

Garcia, D., 2010. Robust smoothing of gridded data in one and higher dimensions with missing values. Comput. Stat. Data Anal. 54, 1167–1178. http://dx.doi.org/10.1016/j.csda.2009.09.020.

Gaudin, D., Delacourt, C., Allemand, P., Jaud, M., Ammann, J., Tisseau, C., Cuq, V., 2009. High resolution DEM derived from thermal infrared images: example of Aber Benoit (France). Geoscience and Remote Sensing Symposium, 2009 IEEE International, IGARSS 2009. Vol. 4. http://dx.doi.org/10.1109/IGARSS.2009.5417474 (pp. IV-705. IEEE).

Guenther, G.C., Brooks, M.W., LaRocque, P.E., 2000. New capabilities of the "SHOALS" airborne LiDAR bathymeter. Remote Sens. Environ. 73 (2), 247–255. http://dx.doi.org/10.1016/S0034-4257(00)00099-7.

Hessner, K., Bell, P.S., 2009. High resolution current & bathymetry determined by nautical X-band radar in shallow waters. OCEANS. 2009-Europe Bremen http://dx.doi.org/10.1109/OCEANSE.2009.5278333.

Hessner, K., Reichert, K., Rosenthal, W., 1999. Mapping of sea bottom topography in shallow seas by using a nautical radar. 2nd Symposium on Operationalization of Remote Sensing Enschede, The Netherlandspp. 16–20 (August, 1999).

Hessner, K., Reichert, K., Borge, J.C.N., Stevens, C.L., Smith, M.J., 2014. High-resolution X-band radar measurements of currents, bathymetry and sea state in highly inhomogeneous coastal areas. Ocean Dyn. 64 (7), 989–998. http://dx.doi.org/10.1007/s10236-014-0724-7.

Heygster, G., Dannenberg, J., Notholt, J., 2010. Topographic mapping of the German tidal flats analyzing SAR images with the waterline method. IEEE Trans. Geosci. Remote Sens. 48 (3), 1019–1030. http://dx.doi.org/10.1109/TGRS.2009.2031843.

Holland, K.T., Holman, R.A., Lippmann, T.C., Stanley, J., Member, A., Plant, N., 1997. Practical use of video imagery in nearshore oceanographic field studies. IEEE J. Ocean. Eng. 22 (1), 81–92. http://dx.doi.org/10.1109/48.557542.

Holman, R.A., Bowen, A.J., 1979. Edge waves on complex beach profiles. J. Geophys. Res. 84 (C10), 6339–6346. http://dx.doi.org/10.1029/JC084iC10p06339.

Holman, R., Haller, M.C., 2013. Remote sensing of the nearshore. Ann. Rev. Mar. Sci. 5, 95–113. http://dx.doi.org/10.1146/annurev-marine-121211-172408.

Holman, R.A., Stanley, J., 2007. The history and technical capabilities of Argus. Coast. Eng. 54 (6–7), 477–491. http://dx.doi.org/10.1016/j.coastaleng.2007.01.003.

Holman, R., Sallenger, A., Lippmann, T., Haines, J., 1993. The application of video image processing to the study of nearshore processes. Oceanography 6 (3), 78–85. http://dx.doi.org/10.5670/oceanog.1993.02.

Ja, S.J., West, J.C., Qiao, H., Duncan, J.H., 2001. Mechanisms of low-grazing-angle scattering from spilling breaker water waves. Radio Sci. 36 (5), 981–998. http://dx.doi.org/10.1029/2000RS002564.

Koopmans, B.N., Wang, Y., 1994. Satellite radar data for topographic mapping of the tidal flats in the Wadden Sea, The Netherlands. Proceedings of the Second Thematic Conference on Remote Sensing for Marine and Coastal Environments, New Orleans. Vol 31.

Liu, Y., Li, M., Mao, L., Cheng, L., Chen, K., 2013. Seasonal pattern of tidal-flat topography along the Jiangsu Middle Coast, China, using HJ-1 optical images. Wetlands 33 (5). http://dx.doi.org/10.1007/s13157-013-0445-6.

Lynch, P.J., Wagner, R.J., 1970. Rough-surface scattering: shadowing, multiple scatter, and energy conservation. J. Math. Phys. 11 (10), 3032. http://dx.doi.org/10.1063/1.1665090.

Lyzenga, D.R., 1985. Shallow-water bathymetry using combined LiDAR and passive multispectral scanner data. Int. J. Remote Sens. 6 (1), 115–125. http://dx.doi.org/10.1109/36.992783.

Mason, D.C., Davenport, I., Robinson, G.J., Flather, R.A., McCartney, B.S., 1995. Construction of an inter-tidal digital elevation model by the "water-line"method. Geophysical Research Letters. 22 (23), 3187–3190. http://dx.doi.org/10.1029/95GL03168.

Mason, D.C., Garg, P.K., 2001. Morphodynamic modelling of intertidal sediment transport in Morecambe Bay. Estuar. Coast. Shelf Sci. 53 (1), 79–92. http://dx.doi.org/10.1006/ecss.2000.0618.

Mason, D.C., Amin, M., Davenport, I.J., Flather, R.A., Robinson, G.J., Smith, J.A., 1999. Measurement of recent intertidal sediment transport in Morecambe Bay using the waterline method. Estuar. Coast. Shelf Sci. 49 (3), 427–456. http://dx.doi.org/10.1006/ecss.1999.0508.

Mattie, M., Harris, D., 1978. The use of imaging radar in studying ocean waves. Coast. Eng. Proc. 1 (16), 174–189. http://dx.doi.org/10.9753/icce.v16.

McCann, D.L., 2007. Dune tracking in the Dee with X-band radar: a new remote sensing technique for quantifying bedload transport. Bangor University, MSc thesis.

McCann, D.L., Bell, P.S., 2014. 2014 marine radar derived current vector mapping at a planned commercial tidal stream turbine array in the Pentland Firth. U.K. MTS/IEEE Oceans 2014 Conference. St Johns, Newfoundland, Canada, pp. 14–19. http://dx.doi.org/10.1109/OCEANS.2014.7003186 (September 2014).

Moore, R.D., Wolf, J., Souza, A.J., Flint, S.S., 2009. Morphological evolution of the Dee Estuary, Eastern Irish Sea, UK: a tidal asymmetry approach. Geomorphology 103, 588–596. http://dx.doi.org/10.1016/j.geomorph.2008.08.003.

Morton, A., Gibeaut, J.C., Paine, J.G., 1995. Meso-scale transfer of sand during and after storms: implications for prediction of shoreline movement. Mar. Geol. 126, 161–179. http://dx.doi.org/10.1016/0025-3227(95)00071-6.

Nicholls, R.L., Marston, A.F., 1939. Shoreline changes in Rhode Island produced by hurricane of September 21, 1938. Bull. Geol. Soc. Am. 50 (9), 1357–1370. http://dx.doi.org/10.1130/GSAB-50-1357.

Nieto Borge, J.C., Guedes Soares, C., 2000. Analysis of directional wave fields using X-band navigation radar. Coast. Eng. 40 (4), 375–391. http://dx.doi.org/10.1016/S0378-3839(00)00019-3.

Nieto Borge, J.C., RodrÍguez, G.R., Hessner, K., González, P.I., 2004. Inversion of marine radar images for surface wave analysis. J. Atmos. Ocean. Technol. 21 (8), 1291–1300. http://dx.doi.org/10.1175/1520-0426(2004)021<1291:IOMRIF>2.0.CO;2.

Nieto Borge, J.C., Hessner, K., Jarabo-Amores, P., de la Mata-Moya, D., 2008. Signal-to-noise ratio analysis to estimate ocean wave heights from X-band marine radar image time series. IET Radar Sonar Navig. 2 (1), 35–41. http://dx.doi.org/10.1049/iet-rsn.

Plant, N.G., Holman, R.A., 1997. Intertidal beach profile estimation using video images. Mar. Geol. 140 (1–2), 1–24. http://dx.doi.org/10.1016/S0025-3227(97)00019-4.

Reichert, K., Hessner, K., Nieto Borge, J.C., Dittmer, J., 1999. WaMoS II: a radar based wave and current monitoring system. Proceedings of ISOPE 1999, Brest. 3, pp. 1–5.

Richards, M.A., 2005. Fundamentals of radar signal processing. McGraw-Hill Education, India.

Rosati, J.D., Kraus, N.C., 2000. Shoal-reduction strategies for entrance channels Coastal Engineering Technical Note CETN-IV-22. U.S. Army Engineer Research and Development Center, Coastal and Hydraulics Laboratory. Vicksburg, MS.

Ryu, J.-H., Won, J.-S., Min, K.-D., 2002. Waterline extraction from Landsat TM data in a tidal flat: a case study in Gomso Bay, Korea. Remote Sens. Environ. 83, 442–456. http://dx.doi.org/10.1016/S0034-4257(02)00059-7.

Ryu, J.-H., Kim, C.-H., Lee, Y.-K., Won, J.-S., Chun, S.-S., Lee, S., 2008. Detecting the intertidal morphologic change using satellite data. Estuar. Coast. Shelf Sci. 78 (4), 623–632. http://dx.doi.org/10.1016/j.ecss.2008.01.020.

Santiago, I. De, Morichon, D., Abadie, S., Castelle, B., Liria, P., Epelde, I., 2013. Video monitoring nearshore sandbar morphodynamics on a partially engineered embayed beach. J. Coast. Res. Spec. Issue 65, 458–463. http://dx.doi.org/10.2112/SI65-078.1.

Senet, C.M., Seemann, J., Flampouris, S., Ziemer, F., 2008. Determination of bathymetric and current maps by the method DiSC based on the analysis of nautical X-band radar image sequences of the sea surface (November 2007). IEEE Trans. Geosci. Remote Sens. 46 (8), 2267–2279. http://dx.doi.org/10.1109/TGRS.2008.916474.

Serafino, F., Lugni, C., Soldovieri, F., 2010. A novel strategy for the surface current determination from marine X-band radar data. IEEE Geosci. Remote Sens. Lett. 7 (2), 231–235. http://dx.doi.org/10.1109/LGRS.2009.2031878.

Sexton, W.j., Moslow, T.F., 1981. Effects on Hurricane David 1979 on the beaches of Seabrook Island South Carolina. Northeast. Geol. 3, 297–305.

Sobral, F., Pereira, P., Cavalcanti, P., Guedes, R., Calliari, L., 2013. Intertidal bathymetry estimation using video images on a dissipative beach. J. Coast. Res. Spec. Issue 65, 1439–1444. http://dx.doi.org/10.2112/SI65-243.1.

Stive, M.J.F., de Schipper, M.A., Luijendijk, A.P., Aarninkhof, S.G.J., van-Gelder-Maas, C., van Thiel de Vries, J.S.M., de Vries, S., Henriquez, M., Marx, S., Ranasinghe, R., 2013. A new alternative to saving our beaches from sea-level rise: the sand engine. J. Coast. Res. 29 (5), 1001–1008. http://dx.doi.org/10.2112/JCOASTRES-D-13-00070.1.

Stone, G.W., Grymes, J.M., Armbruster, C.K., Xu, J.P., Huh, O.K., 1996. Researchers study impact of Hurricane Opal on Florida coast. EOS Trans. Am. Geophys. Union 77 (19), 181–188. http://dx.doi.org/10.1029/96EO00120.

Takewaka, S., 2005. Measurements of shoreline positions and intertidal foreshore slopes with X-band marine radar. Coast. Eng. J. Vol. 47 (Nos. 2 & 3), 91–107. http://dx.doi.org/10.1142/S0578563405001203 (2005).

Trizna, D.B., Hansen, J.P., Hwang, P., Wu, J., 1991. Laboratory studies of radar sea spikes at low grazing angles. J. Geophys. Res. Oceans 96 (C7), 12529–12537. http://dx.doi.org/10.1029/91JC00705 (1978–2012).

Uunk, L., Wijnberg, K.M., Morelissen, R., 2010. Automated mapping of the intertidal beach bathymetry from video images. Coast. Eng. 57 (4), 461–469. http://dx.doi.org/10.1016/j.coastaleng.2009.12.002.

Valenzuela, G., 1978. Theories for the interaction of electromagnetic and oceanic waves—a review. Bound.-Layer Meteorol. 13, 61–85. http://dx.doi.org/10.1007/BF00913863.

van der Wal, D., Forster, R.M., Rossi, F., Hummel, H., Ysebaert, T., Roose, F., Herman, P.M., 2011. Ecological evaluation of an experimental beneficial use scheme for dredged sediment disposal in shallow tidal waters. Mar. Pollut. Bull. 62 (1), 99–108. http://dx.doi.org/10.1016/j.marpolbul.2010.09.005.

Way, O., 2013. The migration of large scale bed forms in the Dee Estuary PhD Thesis University of Bangor, Wales.

Wolf, J., Brown, J.M., Howarth, M.J., 2011. The wave climate of Liverpool Bay—observations and modelling. Ocean Dyn. 6 (5), 639–655. http://dx.doi.org/10.1007/s10236-011-0376-9.

Yoder, N., 2011. PeakFinder(Matlab program). Internet. http://www. mathworks. com-/matlabcentral/fileexchange/25500.

Young, I.R., Rosenthal, W., Ziemer, F., 1985. A three-dimensional analysis of marine radar images for the determination of ocean wave directionality and surface currents. J. Geophys. Res. 90 (C1), 1049–1059. http://dx.doi.org/10.1029/JC090iC01p01049.